Impact of nickel on the surface reaction in ceria-based electrodes for solid oxide cells

F. Kullmann [a,*], D. Esau [a], K. Limbeck [a], S. Dierickx [b], A. Lindner [a], H. Störmer [c], A. Weber [a]

[a] *Institute for Applied Materials (IAM-ET), Karlsruhe Institute of Technology (KIT), D-76131, Karlsruhe, Germany*
[b] *Robert Bosch GmbH, D-70049, Stuttgart, Germany*
[c] *Laboratory for Electron Microscopy (LEM), Karlsruhe Institute of Technology (KIT), D-76131, Karlsruhe, Germany*

HIGHLIGHTS

- Deconvolution of loss processes by distribution of relaxation times.
- Separation of gas diffusion process in GDC based electrodes by nickel infiltration.
- Development of physicochemically meaningful impedance model for GDC fuel electrodes.
- Determination of charge transfer resistance at the GDC-surface by model application.
- Decoration of GDC by nickel nanoparticles improves the charge transfer resistance.

ARTICLE INFO

ABSTRACT

Nickel/ceria composites as fuel electrodes in solid oxide cells have been in focus of research and development for many years. The mixed ionic electronic conductivity and the electrocatalytic activity of the ceria surface improve performance and durability and enable even single-phase ceria fuel electrodes. Previous studies have shown that the performance of the latter is strongly improved by small amounts of nickel. This raises the question to what extend a single-phase ceria fuel electrode is able to provide a suitable performance during an operation at 600–700 °C and how this is affected by nickel.

In this study, gadolinia doped ceria fuel electrodes, whose surfaces were decorated with different amounts of nickel-nanoparticles, are investigated. The nanoparticles were generated by infiltration of nickel nitrate solutions and subsequent thermal annealing. Impedance spectroscopy, DRT-analysis and a transmission line modeling approach were employed to evaluate the charge transfer resistance of differently decorated ceria surfaces. The analysis revealed a strong impact of nickel on the polarization resistance (f = 30 mHz … 10 kHz) improving from 0.196 $\Omega \cdot cm^2$ to 0.05 $\Omega\ cm^2$ at 700 °C or more specifically a reduction of the charge transfer resistance at the GDC-surface of up to two orders of magnitude.

1. Introduction

One of the most promising mixed ionic electronic conductive (MIEC) fuel electrode materials is ceria, typically doped with a rare-earth metal lanthanoid such as gadolinia (GDC) [1] or samaria (SDC) [2]. A special feature of ceria is the electrochemical activity in reducing atmosphere [3,4] which makes it a suitable candidate for a single-phase fuel electrode. Applied in Ni/GDC cermets (ceramic and metal materials) a certain tolerance against sulfur poisoning and carbon deposition was demonstrated which is commonly explained by its MIEC characteristics

and electrochemical activity [5] or by the ability to oxidize sulfur [5–8] and carbon [8]. In the late 1980s Mogensen et al. [4] operated successfully GDC fuel electrodes mixed with yttria stabilized zirconia (YSZ) in methane and hydrogen atmosphere where the possibility of operating the MIEC as a fuel electrode could be demonstrated. Even without an electrocatalyst like nickel or platinum, GDC seems to be electrochemically active in hydrogen atmosphere [9,10] and receives recently interest as a nickel-free fuel electrode in CO_2 electrolysis [11,12]. On the other hand, a pure GDC fuel electrode in a targeted catalyst (Ni, Pt) free environment exhibits a non-acceptable polarization resistance (ASR_{pol})

---

at 750 °C of 138 Ω·cm^2 that was decreased to 27 Ω cm^2 by exchanging the inert gold contact mesh by one made of nickel [13].

To achieve a suitable performance typically high SOFC operating temperatures are necessary. Since a lower operating temperature is more favorable a concept to improve the performance of MIECs was published by Watanabe and co-workers [14–17]. A concept for high performance catalyzed reaction layers by impregnating SDC with small amounts of different noble metals was proposed. The small catalyst particles are assumed to be more active than larger µm-sized nickel in a cermet (for instance Ni/YSZ) and applied on a mixed conducting surface the electrochemical reaction zone is in comparison to a Ni-cermet strongly increased [15]. Based on this work Primdahl et al. [9] infiltrated GDC with small amounts of nickel whereas nickel solely acts as an electrocatalyst. A significant increase in electrode performance with increasing the amount of nickel in the GDC fuel electrode between 0 and 2.5 wt% at temperatures between 700 and 1000 °C could be achieved. The impedance measurements revealed two electrochemical processes. The lower frequency part was assigned to the hydrogen adsorption and/or dissociation on the GDC surface explained by a reduction of the corresponding resistance with a higher nickel amount. The higher frequency part was allocated to the ionic transport in the GDC, whereas the interface YSZ/GDC was excluded due to higher capacity. The electronic transport was assigned to the ohmic resistance [9]. The improvement of the performance by infiltrating nickel in a GDC fuel electrode could be proved by Mirfakhraei et al. [7] and the operating temperature could be lowered down to 500 °C. Next to the performance improvement, a higher tolerance against sulfur compared to GDC without infiltrated nickel was detected explained by nickel acting as a "sulfur adsorber" [7]. The higher tolerance was validated in our recent publication [18,19].

With the trend of operating the solid oxide cell (SOC) at much lower operating temperatures even below 600 °C [20,21] which significantly lowers the electrochemical reaction rates and transport features in conventional electrodes such concepts of nanostructured electrodes are desirable [22–24]. The performance increase is exhibited in different studies applying various nanostructured electrodes achieved by for instance infiltration/impregnation of nitrate solutions in different backbones as fuel electrodes based on Ni/YSZ or (Ni/) GDC [7–9,13,18, 19,25–30] and air electrodes [23,28,31–35]. Osinkin investigated in the last couple of years the influence of nickel and ceria impregnation on different backbones such as Ni/YSZ and a variety of mixed conductors showing the drastic reduction of the polarization resistance [36–40].

In this study we analyze different GDC-based fuel electrodes consisting of a porous sub-µm scaled single phase GDC-layer infiltrated by nickel nitrate solutions with different amounts of nickel nitrate. During thermal annealing and subsequent reduction in a hydrogen atmosphere, nickel nanoparticles were formed.

To our knowledge the impact of nickel nanoparticles on the performance of porous single-phase GDC fuel electrodes is only described by semi-empirical impedance models [7,9,18,19]. In this study the impact of Ni-decoration on the electrochemical reaction at the GDC surface is resolved by a physicochemically meaningful two-channel transmission line model (TLM) [41]. TLMs are commonly used and well accepted to model porous SOC electrodes [12,41–54] and are able to separate and quantify transport and charge transfer related phenomena in porous multiphase electrodes. As in TLM-fitting different combinations of transport and charge transfer parameters provide identical spectra [41, 46], direct fitting results are ambiguous and single parameters as conductivities and microstructural parameters were determined apriori. Fitting the partly pre-parametrized model to the measured impedance spectra revealed a strong impact of the infiltrated Ni-amount on the charge transfer reaction/oxygen exchange at the GDC-surface. A reduction of the corresponding area specific charge transfer resistance at the GDC-surface of up to two orders of magnitude could be achieved by Ni-infiltration.

2. Experimental

2.1. Electrode preparation and SEM analysis

The different electrode variants are applied in symmetrical fuel electrode cells in order to be able to neglect air electrode processes. The electrolyte support consists of an approximately 190 µm thick Y$_{0.16}$Zr$_{0.84}$O$_{2-\delta}$ (8YSZ) substrate manufactured by *ITOCHU Ceratech Corporation, Japan*. The electrode main structure consists of a screen printed (*EKRA-screen-printer, ASYS, Germany*) 20 mol.% gadolinia-doped ceria (Ce$_{0.8}$Gd$_{0.2}$O$_{1.9-\delta}$) layer sintered at 1100 °C for 3 h (*Nabertherm, Germany*). The ink development was conducted by *Forschungszentrum Jülich, Germany*. The particles in the ink exhibited a d$_{50}$ of 0.3 µm. The active cell area is 1 cm^2 in order to reduce gas and temperature gradients within the electrode layer during the electrochemical analysis by electrochemical impedance spectroscopy (EIS). The infiltration of the electrodes was performed at ambient temperature by different water based solutions contained 4.6, 23 and 46 wt% Ni (NO$_3$)$_2$ • 6H$_2$O, explained in appendix A. To guarantee a sufficient in-plane conductivity and a homogenous contact between GDC fuel electrode and contact mesh, the thickness of the sintered GDC layers is 5 µm and a NiO current collector layer (*Kceracell, South Korea*) was applied [19,55]. The different electrode variants are labeled according to "*model cell – type – amount of Ni(NO$_3$)$_2$ · 6H$_2$O in the nitrate solution*" (for instance *MC-B-46*, Table 1).

Cross sections of the different electrode variants were received by scanning electron microscopy (SEM). The cells in the reduced state after testing were cracked in small pieces and deposited by a thin layer of amorphous carbon to reduce charging effects. The imaging was performed with a LEO 1530 (*Zeiss Microscopy, Germany*) applying an accelerating voltage of 5.0 kV. The images feature a combination of 50 % SE2 and 50 % InLens detector.

To investigate the distribution of infiltrated nickel in the GDC fuel electrode, energy dispersive X-ray spectroscopy (EDS) was performed for all type B electrode variants. The samples were embedded in epoxy resin and mechanically polished. To prevent charging, samples were coated with carbon. The analysis was performed with a FEI Quanta FEG 650 (*FEI company, United States*) applying an accelerating voltage of 15.0 kV. EDS mapping was recorded with a *Bruker EDXS Quantax 400 SDD* detector.

2.2. Impedance spectroscopy

To investigate the influence of the infiltrated nickel on the surface reaction the four fuel electrode variants were characterized by EIS. All cells were tested in the identical testbench which is described in Ref. [56]. Both electrodes were contacted with a nickel mesh and a gas flow of 500 sccm in a single gas chamber setup was applied. In order to maximize the comparability between the different electrode variants every cell experienced the same initial conditioning. The cells were heated up to 800 °C in pure nitrogen followed by a reduction procedure by reducing stepwise the ratio of nitrogen and hydrogen towards pure hydrogen, whereby NiO was reduced to Ni. After the reduction process the operating temperature was decreased to 700 °C and the gas mixture was changed to 50 % H$_2$ and 50 % H$_2$O until a stabilization of the

Table 1
Different variants of the fuel electrode and their features.

Label	Ni(NO$_3$)$_2$ • 6H$_2$O	Calculated nickel amount	Electrolyte thickness
	wt.%	vol%	µm
MC-A-0	–	–	188
MC-B-4.6	4.6	0.03	178
MC-B-23	23	0.15	180
MC-B-46	46	0.34	190

impedance was achieved in order to characterize the electrodes afterwards with neglectable ageing effects in moderate conditions up to 30 % H_2O in H_2. The higher humidification was only used to achieve a stable cell performance and is not considered for further characterization since nickel agglomeration is more favored at higher humidification [57].

Impedance measurements were recorded at open circuit voltage (OCV) by a Solartron 1260 in galvanostatic mode. The frequency ranges between 30 mHz and 1 MHz with 12 measurement points per decade which features a good agreement between both resolution and measurement time. The sinusoidal current stimulus was chosen in order to receive a voltage response of the electrode of $\leq$12 mV [56]. Every operating point was measured twice with a delay of 10 min between the measurements in order to be able to detect short term ageing and unstable operating points. To guarantee a sufficient data quality for characterization and DRT calculation the Kramers Kronig validity test [58,59] was used, revealing errors <1 %. For characterization of the electrodes, temperature variations between 600 °C and 700 °C were conducted at different fuel compositions. At the end of each test, sulfur poisoning experiments at 700 °C were conducted. Prior to this, an operation for at least 12 h in 89 %/3 %/8 % $H_2/H_2O/N_2$ without sulfur was conducted, revealing neglectable ageing. The N_2 content is required to enable a similar composition in the subsequent poisoning phase, where N_2 is the carrier gas for H_2S. In the poisoning phase 0.05 ppm H_2S were added for a duration of 24 h. The electrodes exhibit during the complete characterization duration (excluding sulfur poisoning test) a total degradation in ASR_{pol} of <6 % enabling a valid process characterization and model parametrization. To deconvolute the impedance spectra the analysis of the distribution of relaxation times (DRT) [60] was applied followed by a complex nonlinear least squares fit [61] in order to quantify the various loss processes of the different electrode variants. The DRT is calculated from the real part of the impedance spectrum by a fitting approach based on RC-elements [50]. The Fredholm integral is solved by Tikhonov-regularization [62] using a regularization parameter λ of 0.005. Details about our DRT calculation can be found in Refs. [41,50,60,63].

2.3. Four-point dc conductivity measurement

The effective conductivity of the porous GDC-layer was measured in order to determine model parameters. Four-point dc conductivity measurements are applied on a screen printed porous GDC layer ($Ce_{0.8}Gd_{0.2}O_{1.9-\delta}$) sintered on a MgO substrate (*Robert-Bosch-GmbH, Germany*) at 1300 °C for 3 h. For the current input Pt-electrodes were painted, sintered at 1050 °C for 1 h and wired with platinum threads. A

dc current was applied by a Keithley 220 current source whereas the maximum current over the entire layer was chosen in order to obtain a voltage drop below 0.9 V. The voltage measurement between the inner electrodes was performed in a distance of 12 mm. For voltage tap two 0.1 mm Pt-wires were wrapped around the sample twice without using contact paste. A Keysight 34970A digital multimeter was used for recording the data. For further information the authors refer to Ref. [41].

3. Modelling approach and parametrization

In order to quantify the differences in the charge transfer reaction resistance of the different electrode variants a modelling approach based on a two-channel-TLM shown in Fig. 1 c (highlighted in red) is applied [64–66]. This approach is commonly used and well accepted to quantify the electrochemistry, including all charge transport processes and charge transfer reactions occurring inside porous electrodes of different electrochemical devices such as SOCs [12,41–54]. The TLM links the losses caused by ionic and electronic charge transport (r_{ion} and r_{el}) modelled typically as a resistor with the charge transfer reaction (z_{ct}) modelled in our approach as a RQ element. Applying the TLM in common Ni-cermet fuel electrodes the electronic path can be short circuited since the electrodes provide a much higher electronic than ionic conductivity. In our case the transport of electrons and ions take place inside the GDC phase since no percolating nickel matrix is available. In the investigated operation range the electronic resistivity of GDC is just slightly below its ionic resistivity (about one order of magnitude [41]). In many electrodes as LSCF or Ni/YSZ, exhibiting an electronic resistivity that is orders of magnitude below their ionic resistivity, the electronic resistance in the TLM can be neglected and a simplified single channel TLM approach can be applied. For the investigated GDC-electrodes, both ionic and electronic resistivity of the GDC phase have to be considered in the TLM.

The impedance of the two-channel TLM Z_{TLM} is calculated according to equations (1) and (2). The losses allocated to the ionic and electronic transport inside the GDC electrode are entitled as r_{ion} and r_{el} respectively. Losses induced by the charge transfer reaction at the material gas interface are labeled as z_{ct}. The electrode thickness is assigned as L and the ratio between charge transfer impedance and charge transport resistances is named κ (equation (2)).
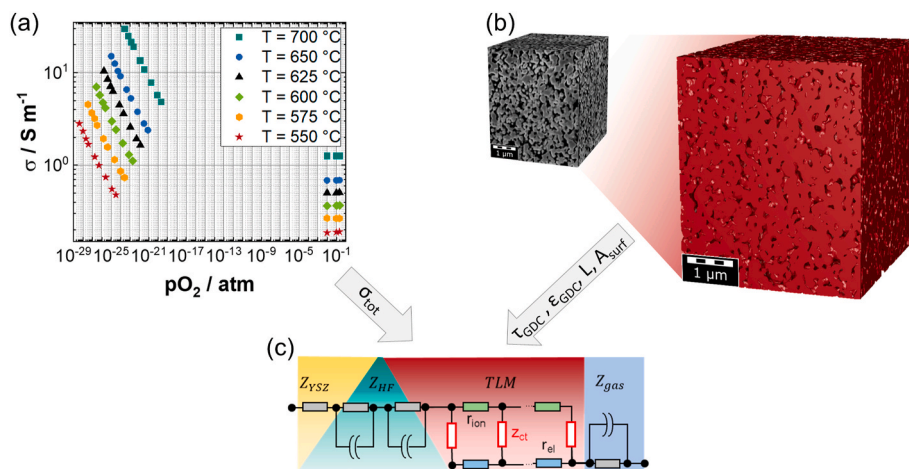

Fig. 1. (a) Total bulk conductivity of GDC σ_{tot} measured at different temperatures and atmospheres. (b) Stack of images and the subsequent 3-D reconstructed volume of the GDC fuel electrode providing microstructural parameters as tortuosity τ and volume fraction ε of the GDC, the thickness L of the GDC layer and the electrochemically active surface A_{surf}. (c) Equivalent circuit model consisting of TLM, RQ elements and a resistor in series.

$$Z_{TLM} = \frac{r_{el} \cdot r_{ion}}{r_{el} + r_{ion}} \cdot \left(L + \frac{2 \cdot \kappa}{\sinh\left(\frac{L}{\kappa}\right)} \right) + \kappa \cdot \frac{r_{el}^2 + r_{ion}^2}{r_{el} + r_{ion}} \cdot coth\left(\frac{L}{\kappa}\right) \quad (1)$$

$$\kappa = \left(\frac{z_{ct}}{r_{el} + r_{ion}} \right)^{1/2} \quad (2)$$

The calculation of the charge transport resistances and the charge transfer impedance are given in equations (3)–(5). $\sigma_{i,GDC}$ describes the ionic and electronic bulk conductivity respectively, A_{act} the active area of 1 cm², τ_{GDC} the tortuosity and ε_{GDC} the volume fraction of GDC. The microstructural parameters τ_{GDC} and ε_{GDC} are defined according to our previous papers [41].

$$r_{ion} = \frac{1}{\sigma_{ion,GDC}(T, pH_2O) \cdot A_{act}} \frac{\tau_{GDC}}{\varepsilon_{GDC}} \quad (3)$$

$$r_{el} = \frac{1}{\sigma_{el,GDC}(T, pH_2O) \cdot A_{act}} \frac{\tau_{GDC}}{\varepsilon_{GDC}} \quad (4)$$

The charge transfer impedance is modelled by a RQ element which represents for every electrode variant a sufficient approach to obtain excellent agreement between measurement and model. It should be considered that more complex models including local inhomogeneities of the electrode could be implemented. A parametrization of this model would be challenging since the analysis and exact quantification of nm-scaled nickel was only possible to a certain extent by SEM analysis methods (secondary electron, EDS, Auger spectroscopy). Especially in the non-infiltrated GDC electrode contacted by Ni current collector (MC-A-0) as shown in Fig. 2 later an exact quantification wasn't possible. Further analysis will be part of future work.

$$z_{ct} = \frac{r_{ct}(T, pH_2O)}{1 + (j\omega\tau_{ct}(T, pH_2O))^{n_{ct}}} \quad (5)$$

The capacity of the charge transfer reaction is calculated by equations (6) and (7) [67].

$$\tau_{ct} = (r_{ct} \cdot Q_{ct})^{\frac{1}{n_{ct}}} \quad (6)$$

$$C_{ct} = \left(r_{ct}^{1-n_{ct}} \cdot Q_{ct} \right)^{\frac{1}{n_{ct}}} \quad (7)$$

The calculation of the error between measurement and model is given in equations (8) and (9):

$$\Delta Z'(\omega) = \frac{Z'_{fit}(\omega) - Z'_{meas}(\omega)}{|Z_{meas}(\omega)|} \quad (8)$$

$$\Delta Z''(\omega) = \frac{Z''_{fit}(\omega) - Z''_{meas}(\omega)}{|Z_{meas}(\omega)|} \quad (9)$$

Since a straightforward fitting of a TLM with open parameters will provide ambiguous parameter sets for the described impedance, it is mandatory to predetermine a number of parameters [41,46]. The flow chart in Fig. 1 visualizes our approach of the model parametrization developed in Ref. [41] which is extended by the gas diffusion impedance in this work.

In our modelling approach the bulk conductivity of GDC (Fig. 1 a), measured between 550 °C and 700 °C in a gas mixture ranging from oxidizing atmosphere (pO₂ = 0.21, 0.1, 0.01) to reducing atmosphere in H₂/H₂O (97 %/3 %–20 %/80 %), and the microstructural parameters obtained from 3D-reconstructed volume of the fuel electrode (b) as well as non-stoichiometry data [68] are used to calculate the TLM parameters r_{ion} and r_{el}, whereas z_{ct} is extracted from the model fit. Further information regarding our parametrization approach of the TLM can be found in Ref. [41].

In serial to the TLM, which describes only charge transfer and transport in the porous GDC-layer, additional equivalent circuit elements to describe the full impedance are necessary as an element for the gas transport, the charge transport via the GDC/YSZ-interface and the series resistance of the electrolyte respectively. The gas transport related losses or generally the gas concentration impedance [69–71] is usually divided in gas diffusion [72] and gas conversion [73]. In case of the 1 cm² cell setup and high gas flow rates applied in this study [56] the gas conversion impedance can be decreased to a no longer detectable value. A common way to describe the impedance of a gas diffusion process inside porous SOC electrodes is the application of a Warburg element [71,72,74,75]. In electrolyte supported cells where the electrode thickness is rather low the assumption is that the diffusion losses are mainly caused by molecular diffusion through the nickel meshes and the flow fields rather than through combined bulk and Knudsen diffusion inside the electrode structure [50,72,76,77]. Both, gas conversion [69, 71] and gas diffusion [50,71] in the gas channels and the Ni mesh applied for contacting can be modelled by a RQ element [50,78]. In our case, we relate the better fitting results for a RQ element instead of a Warburg element to the missing unidirectional gas diffusion related to the in-plane gas diffusion in the Ni contact mesh underneath the contact ribs of the flow field. The distribution of effective gas diffusion lengths no longer meets the assumptions for the Warburg element and the
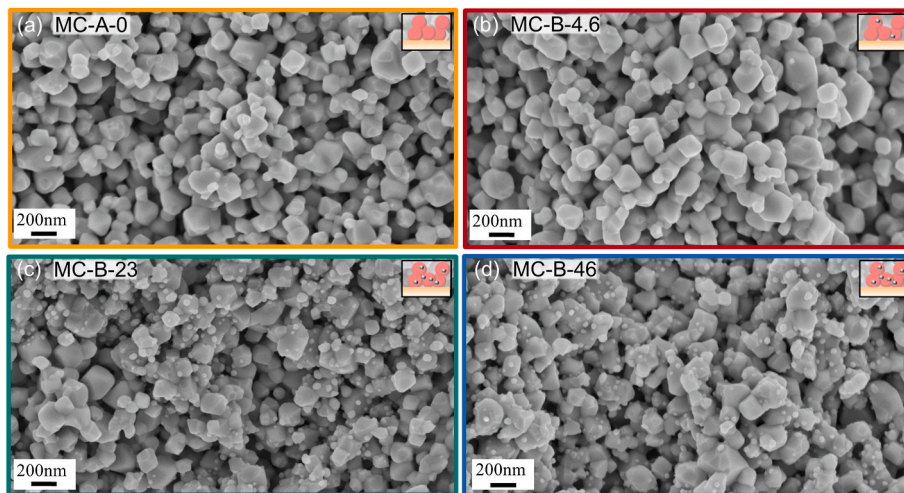

Fig. 2. Post-test scanning electron microscopy cross sections of the non-infiltrated electrode (MC-A-0, a) and the infiltrated electrodes with varying amounts of nickel particles (MC-B-(4.6,23,46), b-d).

distribution of relaxation times in the physicochemically not meaningful RQ element seems to enable a better fit. The same approach was taken by Nielsen et al. [43], applying a RQ element instead of a Warburg element for a better agreement between measurement and model-fit.

Based on the sensitivity analysis discussed later in Fig. 5 and figure C.1 we propose that the peak LF$_{1,B}$ of MC-B-46 is in some operating conditions solely allocated to the gas transport impedance mainly caused by molecular diffusion through the nickel meshes, current collector layer and flow fields rather than the GDC electrode. A calculation of the gas diffusion resistance (Knudsen + bulk diffusion) within the porous GDC layer according to appendix B by equation (B.1) using the microstructural parameters in table B.1 results in $\sim \leq 0.013\ \Omega\ cm^2$.

Since the process LF$_{1,B}$ is only clearly separable from peak LF$_{2,B}$ at high temperatures and relatively low steam contents we extract the total gas diffusion impedance by fitting the pre-parametrized model (by r_{ion}, r_{el} and L) to the impedance spectra of MC-B-46 during a steam variation at 700 °C as shown in Fig. 5 (c). As known from literature the gas diffusion has minor temperature dependency [50,69,70,72] and is here assumed to be constant between 600 °C and 700 °C. The high frequency processes were described by two serial RQ elements and the resistance of the electrolyte by a resistor.

4. Results and discussion

4.1. Structural analysis

Fig. 2 a (yellow) visualizes the cross section of a non-infiltrated GDC fuel electrode (MC-A-0). The smooth surface of the sub-μm scaled GDC indicates that no noticeable amount of nickel diffused from the Ni-current collector layer into the GDC layer during reduction/operation, which is not visible due to limited resolution of the SEM. After infiltration of the lowest amount of nickel-nitrate in the solution (MC-B-4.6) in Fig. 2 b (red) almost no visible change in the cross section is noticeable. Only occasionally single small particles are visible on the GDC surface.

Calculations with the assumption that the pores are completely filled by the solution and no nickel is lost during the following steps reveal a volume fraction of 0.03 vol% metallic nickel (Table 1). Infiltrating a solution with five times more nickel-nitrate into the GDC layer leads to visible nickel nanoparticles on the GDC surface in (c) (green, MC-B-23). A comparison of the left- and right-hand side of (c) could lead to the assumption that the nickel infiltration occurs only locally, but nickel nanoparticles were found in similar amounts all over the electrode from the top of the electrode to the interface between 8YSZ and GDC, but for better visualization of small Ni-particles only a limited part of the electrode is shown in Fig. 2. The infiltration of double the amount of nickel-nitrate (d) (MC-B-46) compared to (c) leads to no visible change in the SEM cross section.

To investigate the distribution of infiltrated nickel in the GDC fuel electrode in more detail, energy dispersive X-ray spectroscopy (EDS) was performed for all type B electrode variants. Fig. 3(a–c) show the EDS mapping of yttria stabilized zirconia in blue and nickel in green. It is noticeable that at the interface between the GDC fuel electrode and the nickel current collector layer (removed during dismounting the cell) on the bottom of each picture, larger nickel particles are occurring especially in MC-B-23 (b). These should be remains from the current collector layer. In the center of MC-B-46 (c) a small area with a stronger nickel signal is detected compared to the rest of the investigated area and could be related to a small hole where more nickel is located. Infiltrated nickel is in average well distributed and similar amounts can be found all over the electrode. It has to be considered that due to low nickel contents, the images are overlapped by noise and an exact quantification of nickel in the GDC electrode ($\leq$0.3 vol%, Table 1) is not possible by EDS in SEM. The intention of this analysis is a visualization of the existence and distribution of Ni, an exact quantification should be avoided. Nonetheless a comparison between the samples is feasible which follows the same trend as the calculated amounts (Fig. 3d and e). Since the electronic conductivity of the GDC fuel electrode is higher than the ionic conductivity but the difference is in the range of about one order of magnitude and lower [41], it is assumed that the location where electrochemical conversion takes place is expanding from the interface electrode/electrolyte towards the electrode [26]. Therefore, it is important that nickel is infiltrated from the top of the electrode until the electrode/electrolyte interface which is the case for every electrode
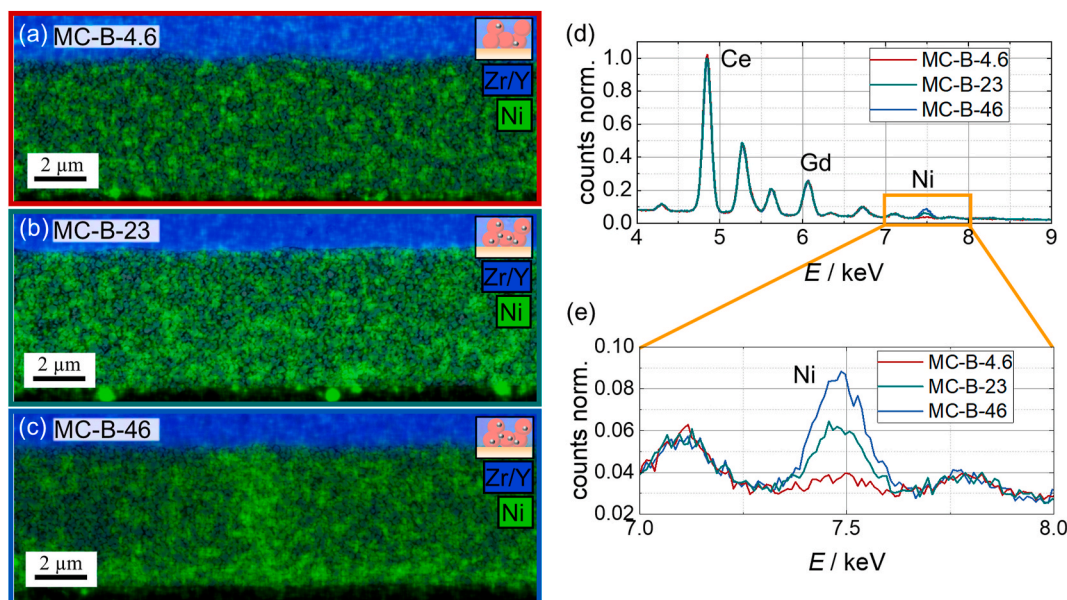

Fig. 3. (a–c) Energy dispersive X-ray spectroscopy cross sections of the infiltrated electrodes with varying amounts of nickel particles (MC-B-(4.6,23,46), top to bottom) to visualize the distribution of the infiltrated nickel in the GDC fuel electrode. The EDS spectra in (d,e) are averaged over the mapped electrode area. The y-axis is normalized to the peak maximum of the Ce peak. The height of the Ni-peak at about 7.5 keV is in good agreement with the infiltrated Ni-amounts. The ratio of the measured atom percentages between those three electrodes is 1:4:8 (MC-B-4.6:MC-B-23:MC-B-46), which matches quite well with the calculated volume percentages of nickel (1:5:11) in Table 1.

variant. Nickel is furthermore detected in the YSZ electrolyte most probably also explainable by noise. The nickel signal in the YSZ seems to increase with lower nickel amount (c over b to a) which supports the explanation.

In order to proof the reproducibility of this manufacturing process in terms of electrode performance, multiple cells of every variant were tested by EIS in the same operation condition. The high reproducibility of the ASR_{pol} of the electrode variants in the impedance spectrum/DRT is exemplarily shown for MC-B-46 in figure D.1 and will be further discussed later.

4.2. Impact of nickel on the polarization resistance

The impact of infiltrated nickel on the electrode performance is analyzed by EIS recorded at the same operating conditions for every cell. Fig. 4 (a, b) picture the impedance spectra (one electrode and half of the electrolyte resistance) and DRTs at 700 °C in 97 %/3 % H_2/H_2O. The low steam pressure maximizes the distance in frequency between the different peaks in the DRT and facilitates a separate analysis in the investigated operating condition. The spectra in Fig. 4 (a) reveal a relative deviation of the ohmic resistances from the mean of all four cells in the range of <5 % which is within the thickness tolerance of the electrolyte (Table 1). But it has to be mentioned that the increase of the ohmic resistance with a higher amount of nickel-nitrate in the solution in type B was reproduced by a second set of cells. The same trend was published by Primdahl et al. [9] at an operating temperature of 850 °C.

The main contribution to the difference in the ohmic resistance is due to different thicknesses of the electrolyte as shown in Table 1. The difference in ohmic resistance for example of MC-B-23 and MC-B-46 can approximately be explained by a 10 μm thicker electrolyte. Additionally, a lower charge transfer resistance leads to less expansion of the reaction zone from the electrode/electrolyte interface towards the electrode resulting in an extended electronic path inside the GDC layer. Since electron transport is usually occurring at high, non-measurable relaxation frequencies [79], it is added to the ohmic resistance. Detailed explanation will be given in section 4.4.

The polarization resistance instead experiences a drastic reduction due to infiltration, although the relative reduction decelerates with a higher amount of nickel. A closer look on the polarization resistance

visualized in the DRT in (b) pictures a drastic decrease of the resistance and increase in frequency in the lower/medium frequency part below 10 kHz whereas the higher frequency part (>10 kHz) shows no systematic trend. This effect on the low frequency peak was also seen in other mixed conductors as $Sr_2Fe_{1.5}Mo_{0.5}O_6$ [36]. According to the process assignment in our previous work [41] about MC-A-0 where the lowest frequency peak was mainly allocated to charge transfer reaction impedance, the small nickel particles on the GDC surface strongly improve the surface reaction. Mirfakhraei et al. [7] assigns the low frequency peak to the rate of H_2 adsorption. When the GDC surface is impregnated by nickel, hydrogen will adsorb on the nickel more quickly compared to GDC [9,26] enabling a hydrogen spillover [80] to the GDC surface where the reaction with oxygen can take place. This additional reaction path is much faster leading to a reduction in resistance [7]. In the presented model all the surface reaction processes are cumulated in the RQ-element designated as one charge transfer reaction. The higher frequency processes were allocated to electrolyte/interface related processes [41] and are minor influenced as expected. At this point we want to give an insight to the reproducibility of the electrode variants exemplary shown for MC-B-46 in figure D.1. The lower frequency part <10 kHz which is in the focus of this work reveals a high reproducibility with $\Delta ASR_{pol} < 1$ % at 700 °C in 97 %/3 % H_2/H_2O. The higher frequency part >10 kHz shows deviations which support the differences in the high frequency part between the electrode variants in Fig. 4.

The largest impact in the lower frequency part of the DRT in Fig. 4 (b) arises from the difference between MC-A-0 and MC-B-4.6. MC-B-23 and MC-B-46 seem to be comparable which might lead to the assumption that saturation is already achieved. Since the difference in the electrochemistry is the focus of this work only the peaks within a frequency range between 30 mHz and 10 kHz were selected for further analysis and displayed as ASR_{pol} in Fig. 4(c and d). Fig. 4 (c) shows the improvement of ASR_{pol} over the infiltrated amount of nickel nitrate in the solution for an operation at 700 °C in 97 %/3 % H_2/H_2O. The resistance of MC-A-0 is improved by almost a factor of three from 0.196 to 0.07 Ω cm^2 with a minor amount of nickel (MC-B-4.6). Further improvement could be realized by a higher amount of nickel particles in MC-B-23 and MC-B-46 which reduced the ASR_{pol} by a factor of four compared to MC-A-0 (0.196–0.05/0.049 Ω cm^2). These results reveal that a minor amount of nickel on the GDC surface already improves the
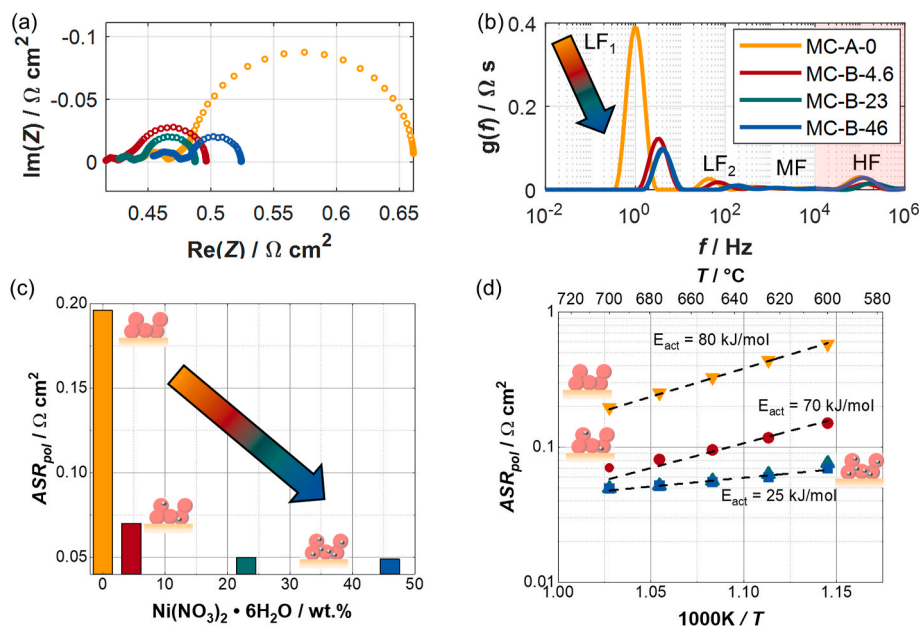

Fig. 4. (a, b) pictures a comparison of the impedance and DRT spectra recorded at 700 °C 97 %/3 % H_2/H_2O of MC-A-0 and MC-B-(4.6,23,46) leading to the assumption that with a higher amount of nickel the surface reaction is improved. (c) visualizes the change in polarization resistance (ASR_{pol}) over Ni(NO$_3$)$_2$ • 6H$_2$O at 700 °C 97 %/3 % H_2/H_2O and (d) exhibits the extracted ASR_{pol} over temperature in 97 %/3 % H_2/H_2O of the different electrode variants.
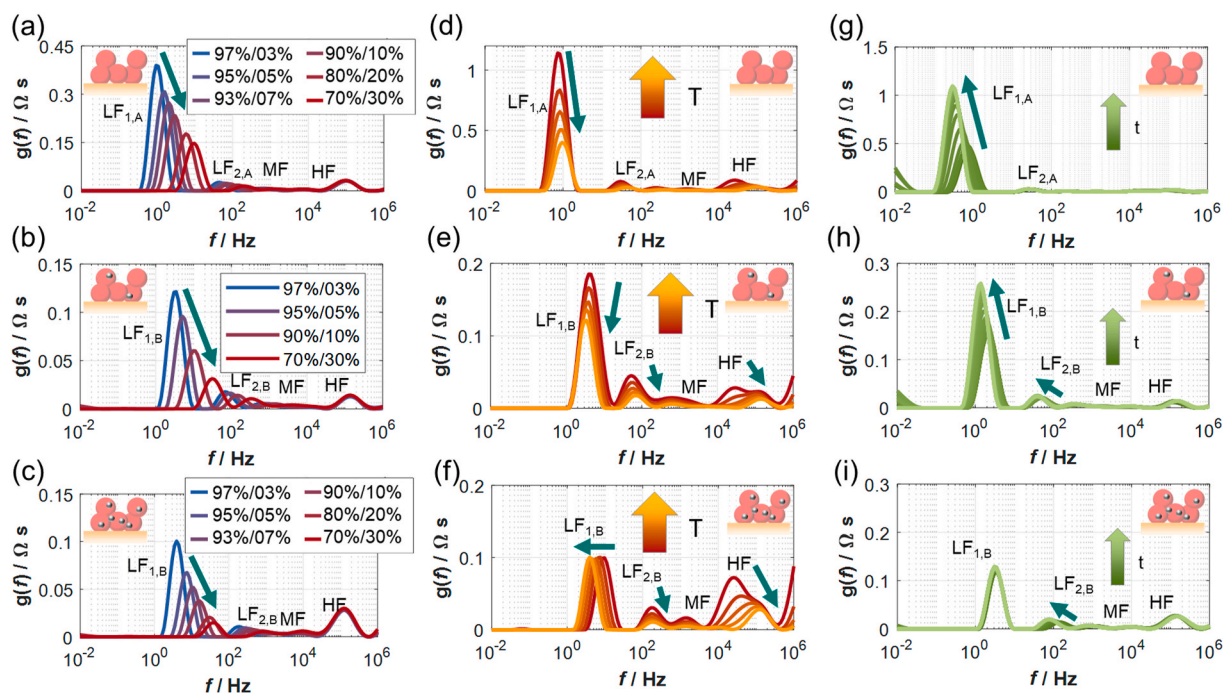
Fig. 5. Sensitivity analysis of three electrode variants (a, d, g: MC-A-0; b, e, h: MC-B-4.6; c, f, i: MC-B-46). (a–c) Steam variation balanced with hydrogen at a constant temperature of 700 °C from 97 %/3 %–70 %/30 % H_2/H_2O. The polarization resistance (ASR_{pol}) decreases strongly which is mainly influenced by two low frequency peaks pictured in the DRT. (d–f) To identify thermally activated processes in the impedance spectra a variation of the temperature from 600 °C to 700 °C in 25 K steps in a constant gas atmosphere containing 97 % H_2 and 3 % H_2O is performed. Except of the resistance of peak $LF_{1,B}$ in (f) every peak seems to be thermally activated. (g–i) The allocation of the charge transfer reaction is supported by a sulfur poisoning test at 700 °C in 89 %/3 %/8 % $H_2/H_2O/N_2$ with 0.05 ppm H_2S. The impedance evolution of the ASR_{pol} over time visualized in the DRT shows that the location of major impact changes its frequency between the electrode variants.

electrode performance significantly whereas a further increase of the nickel amount results only in a minor performance increase.

It has to be considered that the non-infiltrated GDC fuel electrode (MC-A-0) shows a highly reduced ASR_{pol} compared to a previously investigated GDC electrode operated in a "Ni-free" environment at 750 °C (138 Ω cm^2) [13]. This reduction of the ASR_{pol} can be partly attributed to the application of a current collector layer which ensures a complete activation of the whole electrode area. Assuming that the GDC electrode operated in a "Ni-free" environment [13] is only partly activated due to high in-plane resistance of the GDC, leads to an *ASR*-value of 3.27 Ω cm^2 after a calibration via the ohmic resistance which is still higher than the values measured in this work. So, a diffusion of nickel from the current collector into the GDC fuel electrode has to be considered [81] providing an activation of the GDC surface and a lower ASR_{pol}.

Fig. 4 (d) pictures the difference in the thermal activation of the ASR_{pol} of the different electrode variants. Whereas MC-A-0 shows an Arrhenius behavior with an activation energy of 80 kJ/mol, the thermal activation of the ASR_{pol} of type B is strongly reduced explained by a transition of the dominating loss process in the analyzed frequency range [77]. The ASR_{pol} includes thermally activated losses in the GDC-electrode and gas diffusion losses in the gas channels and the Ni contact mesh. The gas diffusion impedance has only a minor temperature dependency and should not be affected by the amount of nickel. Thus, it should be identical for all investigated samples. On the other hand, the electrochemistry is expected to be highly dependent on temperature and Ni-amount. The high activation energy of MC-A-0 is related to the high charge transfer resistance in this GDC fuel electrode which is dominating over the gas diffusion resistance [41]. Towards a higher amount of nickel in the GDC fuel electrode the charge transfer resistance is assumed to decrease whereas the gas diffusion polarization is not affected. Thus, the gas diffusion gets more and more dominant with increasing Ni-content and temperature and lowers the temperature dependency of the ASR_{pol}. It should be noted that under such conditions,

the determination of an activation energy is not meaningful as the ASR_{pol} is affected by the different temperature dependencies of different loss processes in the cell.

To get a better understanding of the different processes in the impedance spectra of the electrode variants a sensitivity analysis will be discussed in the following section. Since MC-B-23 and MC-B-46 have similar resistances only three electrode variants MC-A-0, MC-B-4.6 and MC-B-46 are part of the sensitivity analysis.

4.3. Sensitivity analysis

The ASR_{pol} obtained above includes the losses induced by different processes. To correlate the impact of nickel to the charge transfer resistance solely, a physicochemically motivated TLM approach is used. Before applying and parametrizing the model a comprehensive understanding of the electrochemical behavior of the fuel electrodes is mandatory, which is obtained by a sensitivity analysis. It includes three operating parameter variations of the non-infiltrated (MC-A-0), the minor infiltrated (MC-B-4.6) and the strongly infiltrated GDC electrode (MC-B-46) presented in Fig. 5. It has to be considered that for better visualization the y-axis presenting type B are scaled down.

Fig. 5(a–c) pictures a steam variation balanced with hydrogen at 700 °C. The gas mixture ranges from 97 %/3 % H_2/H_2O to 70 %/30 % H_2/H_2O (blue to red). All three electrode variants show a comparable trend of the different peaks. Whereas the lower frequency peaks LF_{1+2} decrease in resistance and increase in frequency towards higher steam, the higher frequency part shows minor impact. The peaks in the lower frequency range are often allocated to the electrochemistry overlapped by gas diffusion losses and show the expected behavior. The trend of peak LF_1 is in accordance with literature studies of Ni/GDC cermets [76, 77,82] and porous single-phase GDC electrodes infiltrated with nickel or only contacted by a nickel current collector layer [9,41]. The in our study observed decrease of the peak height related to the surface reaction is furthermore in accordance with investigations of doped ceria thin

films [83–85]. The behavior of LF$_2$ varies in literature between neglectable change and decrease of the resistance with a higher steam concentration [41,76,77,82,86]. The peaks in the medium frequency range are less influenced. The high frequency part shows minor dependency of the gas mixture and is assumed to be related to the electrolyte [79,87,88] and/or the interface [89–92] between the GDC fuel electrode and the YSZ electrolyte. Since these processes are not in the focus of this study we refer to Ref. [79] where a detailed discussion about electrolyte related processes in electrolyte supported cells and the relation between conductivity and relaxation frequency is explained.

Fig. 5(d–f) pictures a temperature variation between 600 °C and 700 °C in 25 K steps performed in a constant gas mixture of 97 %/3 % H$_2$/H$_2$O. The polarization resistance of MC-A-0 reveals in the DRT (d) only thermally activated peaks arising from an overlap of the gas diffusion process and the charge transfer reaction in the lowest frequency peak LF$_{1,A}$ [19,41,76,77,86,93]. This overlap is usually assigned to a large volumetric chemical capacity of ceria [41,76,77,82,86,94] which decreases the characteristic frequency of the charge transfer reaction. The peak LF$_{1,B}$ of MC-B-4.6 (e) changes its behavior in frequency compared to LF$_{1,A}$ in MC-A-0. In the non-infiltrated GDC electrode (MC-A-0) the frequency shifts slightly from lower to higher frequencies with increasing temperature as expected for a thermally activated process (frequency $\sim 1/(R*C)$) assuming the change in capacity C is minor than the reduction in resistance R. In MC-B-4.6 the peak shifts from higher to lower frequencies with increasing temperature. The rest of the peaks show a comparable behavior to MC-A-0. In MC-B-46 (f), the GDC electrode with the highest amount of infiltrated nickel, the resistance of peak LF$_{1,B}$ is no more temperature activated and the shift in the frequency has the same direction as in (e). Whereas the resistance remains constant the capacity seems to increase displayed as a shift in relaxation frequency towards lower frequencies ($\Delta f = 5$ Hz). A temperature variation of MC-B-46 at much higher temperatures between 750 °C and 850 °C in 97 %/3 % H$_2$/H$_2$O in figure C.1 showed a minor deactivation of peak LF$_{1,B}$ with higher temperature which is typical for a gas diffusion impedance [50]. Since the electrode experienced minor ageing during this high temperature operation (up to 900 °C) the measurements were not considered for further interpretation, but it is taken as a proof for a well separated gas diffusion impedance in peak LF$_{1,B}$ of MC-B-46. The frequency shift in Fig. 5 (f) compared to figure C.1 might be explained by the distance between both low frequency peaks (LF$_{1,B}$ and LF$_{2,B}$) which decreases towards lower temperature. So, the proximity of both could lead to an interaction due to the Tikhonov regularization in the DRT-calculation and might shift the peak LF$_{1,B}$ towards higher frequencies.

These two operating parameter variations imply that the peak LF$_{1,A}$ in the non-infiltrated electrode visualizes the characteristic overlap of gas diffusion (minor contribution) and charge transfer reaction (dominating process within the peak) as schematically shown in the DRT of Ni/GDC cermets in Ref. [54]. Towards higher amounts of nickel the charge transfer reaction shifts towards higher frequencies and influences the peak LF$_{1,B}$ to a fewer amount until the gas diffusion impedance is completely separated in MC-B-46 at specific operating conditions.

To prove the location of the charge transfer reaction in the impedance spectra a sulfur poisoning test with 0.05 ppm H$_2$S at 700 °C in 89 %/3 %/8 % H$_2$/H$_2$O/N$_2$ was conducted (Fig. 5g–i). In this study the poisoning test is only used as a tool to locate the charge transfer process. An analysis about the sulfur poisoning and regeneration behavior of GDC electrodes can be found in Ref. [19]. The relatively low amount of H$_2$S which is less than expected for a real SOFC system operated with hydrocarbon fuels [95] is chosen to decelerate the impact of poisoning and to reduce the change in the impedance spectrum in regards to an easier process assignment. It is well known that the electrocatalyst, in this case nickel, is strongly affected by small amounts of sulfur in the fuel gas as shown in many studies for different Ni-based fuel electrodes as Ni/YSZ and Ni/GDC [5,25,30,94,96–105] and GDC electrodes contacted by nickel current collector [18,19]. The poisoning results in a strong

increase of the charge transfer resistance and is therefore a useful technique to localize this process.

All three electrode variants show the expected increase of the ASR_{pol} over time, but the frequency range where it occurs differs. The DRT of MC-A-0 (g) shows the expected behavior of a ceria-based fuel electrode with an increase of the lowest frequency peak LF$_{1,A}$ [18,19,25,94,104, 105] which usually represents the charge transfer reaction losses that are overlapped by minor gas diffusion losses. In MC-B-4.6 in (h) LF$_{2,B}$ seems to be minor impacted as well next to the main impact on LF$_{1,B}$. In MC-B-46 on the other hand LF$_{1,B}$ remains almost constant whereas LF$_{2,B}$ increases strongly. This proves the hypothesis that the charge transfer reaction is shifted in frequency from LF$_{1,A}$ in MC-A-0 to LF$_{2,B}$ in MC-B-46.

The results of the poisoning test presented here support the allocation of gas diffusion impedance in LF$_{1,B}$ and charge transfer reaction in LF$_{2,B}$ in MC-B-46 as indicated from the temperature variation. The adjacent peaks to the charge transfer reaction (LF$_{2,A}$, MF$_{A,B}$) are mainly allocated to the charge transport inside the GDC layer because of the transmission line behavior of the porous electrodes and the independency on sulfur poisoning. The high frequency part >10 kHz is assigned to interface and electrolyte related processes. The process assignment of MC-A-0 and MC-B-46 is summarized in Table 2. The low frequency peaks of MC-B-4.6 seem to have a transition regarding the underlying processes and needs further analysis by TLM.

To analyze and quantify the different processes of electrochemistry (charge transport and charge transfer reaction) and gas diffusion separately, the parameters of the physicochemically motivated TLM will be investigated in the following.

4.4. Model validation

In order to ensure reliability of the model parameters, the model is validated by the impedance spectra of the different electrode variants. Combining the generated parameter sets including the TLM input parameters r_{ion} and r_{el} (equation (3) and (4)) as well as L and the gas diffusion resistance (determined from MC-B-46) in the presented model in Fig. 3 (c), an excellent fit quality with an error <1 % (30 mHz until 10 kHz) shown in Fig. 6 can be achieved and an extraction of the charge transfer resistance r_{ct} can be performed.

The measurement is plotted as grey circles in the Nyquist diagram and as a grey dashed line in the DRT (Fig. 6). The fit is visualized in both diagrams by a black line. It has to be considered that for better visualization the axis presenting type B are scaled down. The single equivalent circuit elements are pictured in the Nyquist diagram as well as in the DRT. The high frequency processes related to the interface are colored in green. The TLM describing the electrochemistry is colored in red whereas the gas diffusion impedance is depicted in blue.

The DRT of the non-infiltrated GDC electrode MC-A-0 in (Fig. 6 b) shows an overlap of gas diffusion impedance and charge transfer reaction in LF$_{1,A}$ as known from Ni/GDC cermets [54]. In the presented operating condition the gas diffusion impedance is comparably low and

Table 2
Peaks in the impedance spectra/DRT and corresponding process assignment of the dominating processes of MC-A-0 and MC-B-46.

Peak	Dependencies	Physical process
LF$_{1,A}$	T, pH$_2$/pH$_2$O, H$_2$S	Charge transfer reaction + minor gas diffusion contribution
LF$_{2,A}$	T, pH$_2$/pH$_2$O	Charge transport in the electrode
LF$_{1,B}$	T, pH$_2$/pH$_2$O	Gas diffusion (only visible in electrode with high Ni-content)
LF$_{2,B}$	T, pH$_2$/pH$_2$O, H$_2$S	Charge transfer reaction (only visible in electrode with high Ni-content)
MF	T, pH$_2$/pH$_2$O	Charge transport in the electrode
HF	T	Ionic transport via the GDC/8YSZ-interface
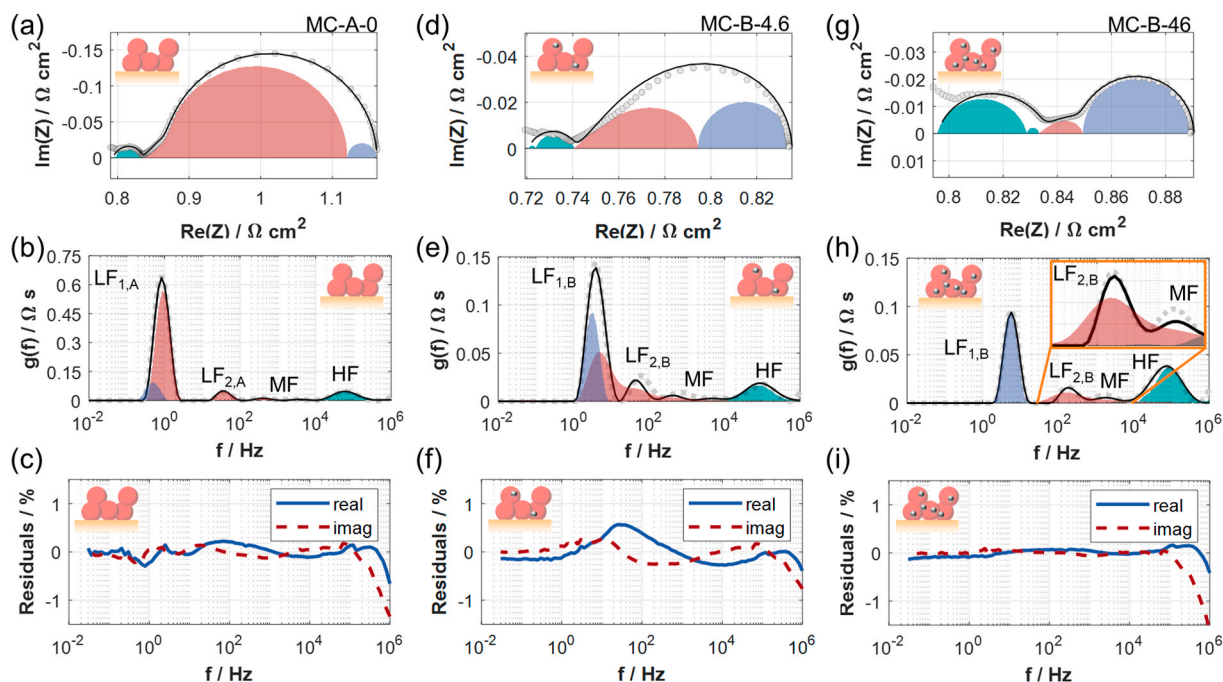
Fig. 6. Fitting results of a variation of the nickel amount in GDC electrodes at 650 °C in 97 % H_2 and 3 % H_2O. Whereas the gas diffusion resistance is kept constant for every cell, the charge transfer process decreases in resistance and increases in frequency from (a–c) MC-A-0 over (d–f) MC-B-4.6 to (g–i) MC-B-46.

therefore the behavior of the peak is mainly dominated by the charge transfer reaction explaining the temperature dependency of peak $LF_{1,A}$ in Fig. 5 (d). By infiltration of a minor amount of nickel in MC-B-4.6 (Fig. 6d–f) the charge transfer resistance is improved and the characteristic frequency is slightly shifted towards higher frequencies (axis are scaled down). Due to the lower resistance the gas diffusion impedance is now more dominating the peak $LF_{1,B}$ and subsequently the behavior of the peak during the temperature variation in Fig. 5 (e) changes. With the highest amount of nickel in the GDC fuel electrode in MC-B-46 (Fig. 6g–i) the charge transfer resistance decreases even more and shifts once again to much higher frequencies. In this case the gas diffusion impedance ($LF_{1,B}$) is visible as a separate peak. The transition in MC-B-4.6 from a charge transfer dominated peak $LF_{1,A}$ in MC-A-0 to a gas diffusion dominated peak $LF_{1,B}$ in MC-B-46 was successfully resolved by the application of the physicochemically motivated impedance model and a deconvolution of the gas diffusion impedance and the electrochemistry is possible.

The shape of the electrochemistry (TLM, red) in the Nyquist diagram in Fig. 6(a, d, g) indicates as well the variation of the ratio between charge transfer impedance and charge transport resistance (κ, equation (2)) of the different electrode variants which is usually a measure for the penetration depth in a one channel TLM [42]. In MC-A-0 (a) the shape of the TLM impedance is similar to an RQ element with a kink at high frequency which exhibits that the impedance due to charge transfer reaction is increased compared to the charge transport resistances resulting in a high κ. In this case the value of κ could even exceed the electrode thickness. With an infiltration of nickel in type B the Nyquist diagram of the TLM is more similar to a Gerischer shape. This indicates that the ratio between the charge transfer impedance and the charge transport resistances (κ) becomes much smaller than the electrode thickness [41,42,106,107]. Since the charge transport resistances are unaffected by the nickel amount the transition of the shape is solely attributed to the change in charge transfer impedance. With constant charge transport resistances and a reducing charge transfer impedance the reaction should occur closer to the electrolyte with a higher amount of nickel (κ decreases). If the penetration depth is smaller, the electrons have to travel a longer way inside the GDC fuel electrode leading to a higher ohmic resistance, but the resistance increase is in our case in

comparison to the impact of the electrolyte thickness about one order of magnitude lower.

4.5. Model application

In order to investigate the improvement of the charge transfer reaction resistance by a higher amount of nickel more in detail, the same temperature variation in 97 %/3 % H_2/H_2O as already investigated in Fig. 4 by comparing the ASR_{pol} is now analyzed by the application of the developed TLM-based impedance model.

Fig. 7 pictures the quality of the model-fit (grey line) on the impedance data exemplary for a steam variation balanced with hydrogen at a constant temperature of 700 °C from 97 %/3 %–70 %/30 % H_2/H_2O. The maximum error between model-fit and measurement is for every operating point less than 1 % within the investigated frequency range from 30 mHz until 10 kHz and is therefore suitable for further analysis. The shift of the ohmic resistance to higher resistances with increasing pH_2O and pO_2 is not allocated to the YSZ electrolyte, but to the charge transport in the GDC fuel electrode.

The extracted r_{ct} of the impedance data recorded at different operating temperatures is shown in Fig. 8. (a) reveals the r_{ct} at 700 °C in 97 %/3 % H_2/H_2O of every electrode variant. Comparing the results with the analysis of the ASR_{pol} in Fig. 4 underlines the requirement of a physicochemically motived impedance model. The improvement from the non-infiltrated electrode (MC-A-0) towards the electrode type B is even more significant than expected from the ASR_{pol}. Whereas the ASR_{pol} reveals an improvement by a factor of four, the charge transfer resistance was improved by about two orders of magnitude explained by excluding gas diffusion and charge transport from the extracted resistance. Even the charge transfer resistance in the minor infiltrated electrode MC-B-4.6 is reduced by nearly one order of magnitude compared to the non-infiltrated GDC electrode. The activation energies (b) which were determined by a linear regression in the logarithmic y-scale show comparable values (within the accuracy of the fit) for all electrode variants. The comparability of the activation energies is supported by a comparison of pristine and nickel decorated GDC20 thin films [83] whereby the values are slightly lower which might be explained by a different gas mixture.
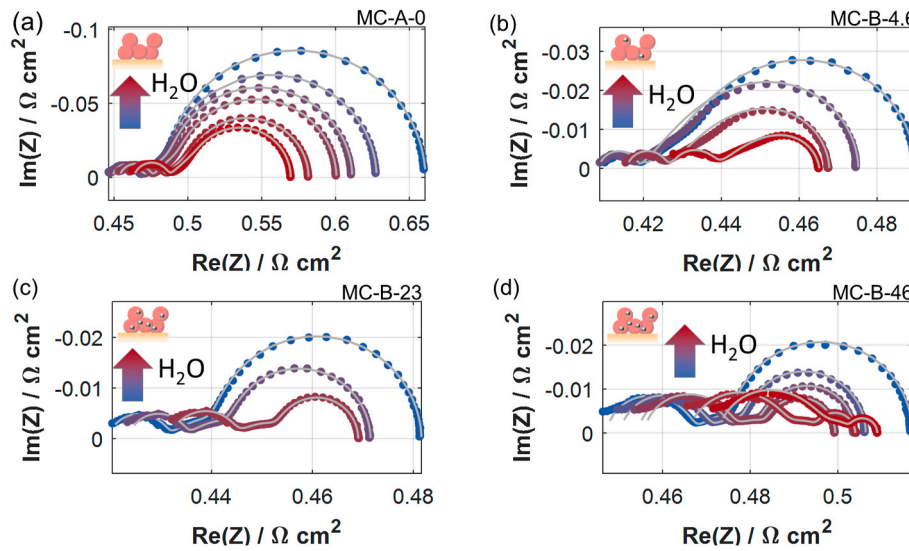
Fig. 7. Model-fit (grey line) and measurements of the different electrode variants are in good agreement during a steam variation balanced with hydrogen at a constant temperature of 700 °C from 97 %/3 %–70 %/30 % H₂/H₂O (a: MC-A-0; b: MC-B-4.6; c: MC-B-23; d: MC-B-46). (c includes only the variation between 97 %/3 %–90 %/10 % H₂/H₂O).
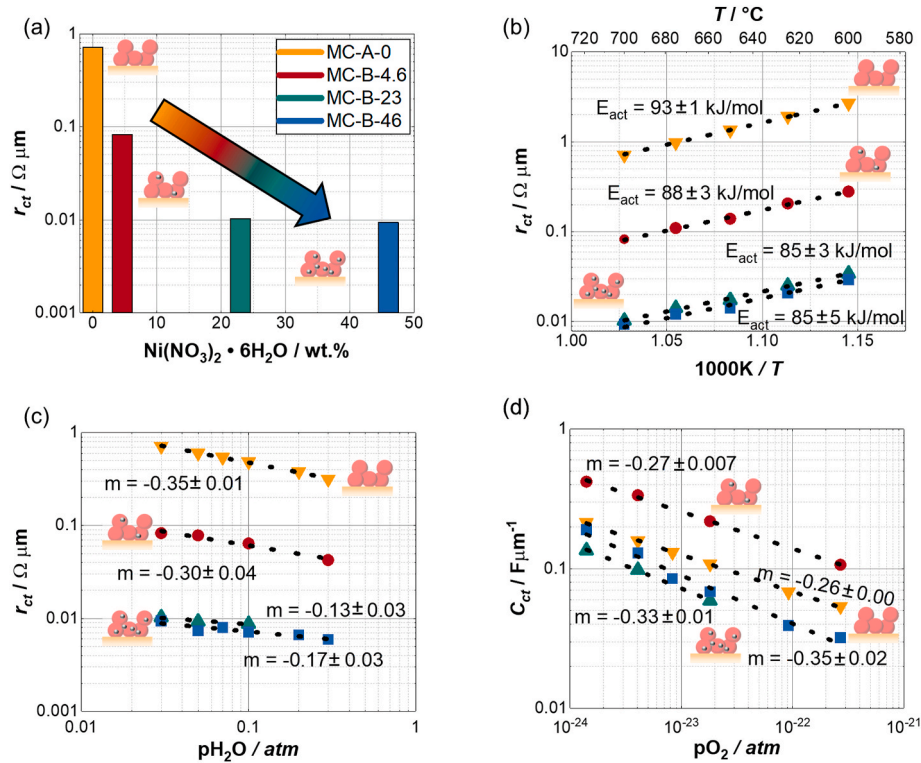

Fig. 8. (a) visualizes the change in charge transfer resistance (r_{ct}) over Ni(NO₃)₂ • 6H₂O at 700 °C in 97 %/3 % H₂/H₂O and (b) exhibits the extracted r_{ct} over temperature in 97 % H₂ and 3 % H₂O. A reduction of the corresponding losses of about two orders of magnitude are achieved by infiltrating low amounts of nickel. (c) visualizes the r_{ct} during steam variation balanced with hydrogen at 700 °C and (d) the capacity of the charge transfer reaction.

The steam variation between 3 % and 30 % steam balanced with hydrogen at 700 °C (c) shows comparable dependencies of the charge transfer resistance of MC-A-0 and MC-B-4.6 and is in accordance with GDC and SDC thin films measured at 650 °C [83,84] with dependencies around −0.3 to −0.4. The higher infiltrated electrodes reveal lower dependencies. The pO₂ dependency of the chemical capacity of doped ceria and the capacity of the surface reaction is given in literature with −1/4 [12,83,108–110], which is in accordance with our investigations for the capacity of the charge transfer reaction (calculated by equation

(6) and (7)) of MC-A-0 and MC-B-4.6 in (d). The dependency of the capacity of the highly infiltrated electrodes (MC-B-23 and MC-B-46) seems to be a bit higher than of the non-infiltrated electrode.

The difference in the total capacity and the slope of capacity and resistance over pH₂O and pO₂ could be explained by a difference in the single reaction mechanisms. The RQ element in the TLM describes all the processes occurring during the surface reaction like H₂ adsorption and dissociation, electron transfer and desorption of steam [111,112], which might be more or less influenced by the addition of nickel. It represents

one volume specific capacity and resistance homogenized over the whole electrode. The capacity for instance includes to a significant amount the chemical capacity of GDC, but furthermore also double layer capacities and electrical capacities which could be influenced differently by the addition of nickel.

To verify the extracted charge transfer resistance and to be able to classify the performance, a comparison to different cell types in literature is conducted. The non-infiltrated GDC electrode (MC-A-0) operated at 700 °C in 97 % H_2 and 3 % H_2O shows a comparable charge transfer resistance to a high temperature fuel electrode supported cell with an active electrode made out of Ni/8YSZ operated at 800 °C (designated operating temperature) in 94.5 % H_2 and 5.5 % H_2O [44]. Furthermore a Ni/GDC cermet [45] operated at 650 °C reveals charge transfer resistance values in a similar range as the MC-A-0 electrode. A Ni/GDC fuel electrode applied in an ESC designated for operation temperatures up to 860 °C exhibited at 860 °C a charge transfer resistance comparable to MC-A-0/MC-B-4.6 at 700 °C [54]. The charge transfer resistance of a GDC infiltrated metal supported cell [43] operated at the same operation conditions at 650 °C and 700 °C has a higher charge transfer resistance than MC-A-0. The same metal supported cell was also infiltrated by Ni:GDC [43] revealing resistances between MC-A-0 and MC-B-4.6.

With the physicochemically motivated TLM developed in this work we were able to quantify the charge transfer resistance of the GDC-surface and its improvement by nickel decoration. Our analysis revealed that Ni-infiltration improves the charge transfer resistance at the GDC-surface by up to two orders of magnitude in the investigated operation conditions. Compared to other cell designs and fuel electrode materials investigated by TLMs our highly infiltrated GDC fuel electrode reveals a comparably low charge transfer reaction resistance.

5. Conclusions

The aim of this study was to quantify the improvement of the charge transfer reaction resistance in GDC fuel electrodes by decorating the GDC-surface with minor amounts of unconnected nickel. For this purpose, symmetrical cells were manufactured and investigated by electrochemical impedance spectroscopy, energy dispersive X-ray spectroscopy and scanning electron microscopy. The nickel particles were generated by infiltration and subsequent thermal annealing of nickel-nitrate solutions and lead to an improvement of the polarization resistance (f = 30 mHz … 10 kHz) by a factor of four from 0.196 $\Omega \cdot cm^2$ to 0.05 mΩ cm^2 at 700 °C in 97 %/3 % H_2/H_2O.

Applying DRT analysis to different operating parameter variations revealed two low frequency peaks, smaller peaks in the medium frequency range and a larger peak at high frequencies. The two low frequency and the medium frequency peaks could be allocated to the gas diffusion and electrochemistry of the fuel electrode. The electrochemistry includes charge transport processes and charge transfer reactions occurring inside the porous electrode described by a transmission line

modeling approach. The higher frequency part is assigned to interfacial losses. Whereas electrodes with low amount of nickel showed the typical overlap of electrochemistry and gas diffusion, electrodes with high nickel content allowed a separation of both loss processes and enabled a separated analysis.

The application of the two-channel transmission line model revealed an excellent agreement between measurement and model-fit with errors below 1 %. For parametrization of the model FIB-SEM tomography followed by a 3D-reconstruction combined with 4-point dc measurements to collect the charge transport resistances in the GDC fuel electrode and impedance spectroscopy to determine the gas diffusion impedance were conducted. The pre-parametrized model applied on the impedance spectra of the different electrode variants enabled an extraction of the charge transfer resistances at the Ni-decorated GDC-surfaces. An improvement by two orders of magnitude from 0.7 $\Omega \cdot \mu m$ to 0.009 Ω μm at 700 °C in 97 %/3 % H_2/H_2O comparing the non-infiltrated GDC electrode with the highly infiltrated one could be achieved.

CRediT authorship contribution statement

F. Kullmann: Writing – original draft, Visualization, Validation, Software, Project administration, Methodology, Investigation, Formal analysis, Data curation, Conceptualization. **D. Esau:** Writing – original draft. **K. Limbeck:** Investigation. **S. Dierickx:** Writing – original draft, Conceptualization. **A. Lindner:** Visualization, Investigation. **H. Störmer:** Investigation. **A. Weber:** Writing – original draft, Supervision, Methodology, Funding acquisition, Conceptualization.

Declaration of competing interest

The authors declare that they have no known competing financial interests or personal relationships that could have appeared to influence the work reported in this paper.

Acknowledgments

Appendix A

The nickel nitrate solutions are based on a mixture of nickel hexanitrate ($Ni(NO_3)_2 \bullet 6H_2O$) and demineralized water. The amount of nickel hexanitrate was varied (4.6, 23 and 46 wt% $Ni(NO_3)_2 \bullet 6H_2O$).

For infiltration of the electrodes, the samples were placed in a beaker glass inside a vacuum chamber (*CitoVac, Struers, Germany*) at ambient temperature and in 200 mbar absolute pressure. After a waiting period of 10 min at this pressure the cells were flooded by the nitrate solution until the cells are completely covered. After going back to ambient pressure, a waiting period of 2 min followed. The cells were then taken out of the solution and dried in a drying cabinet for 24 h at 70 °C. The calcination process took place in a furnace (*Nabertherm, Germany*) at 400 °C for 3 h in air, where $Ni(NO_3)_2 \bullet 6H_2O$ converts to NiO.

Appendix B

The gas diffusion resistance within the porous GDC fuel electrode is calculated according to Ref. [113] and given in equation (B.1).

$$R_{gas} = \left(\frac{R \cdot T}{2 \cdot F}\right)^2 \cdot \frac{L_{fe} \cdot \tau_{pore}}{\varepsilon_{pore}} \cdot \left(\frac{1}{D_{mol,H_2} \cdot pH_2} + \frac{1}{D_{mol,H_2O} \cdot pH_2O}\right) \cdot \left(1.0133 \cdot 10^5 \frac{Pa}{atm}\right)^{-1} \tag{B.1}$$

R denotes the universal gas constant, T the absolute temperature, F the faraday constant and $D_{mol,i}$ the molecular diffusion coefficient for H_2 and H_2O respectively, calculated by the Bosanquet-approach using bulk and Knudsen diffusion coefficients [113]. The microstructural parameters of GDC and pore volume are determined as described in Ref. [41] by GeoDict [114] and listed in table B.1. The tortuosity given here is in GeoDict [114] designated as tortuosity factor [115].

The application of equation (B.1) and the microstructural parameters in table B.1 result in a gas diffusion resistance (Knudsen + bulk diffusion) within the porous GDC layer of 0.013 Ω cm^2 at 700 °C and 97 %/3 % H_2/H_2O which features the highest gas diffusion resistance in the investigated operation conditions from 700 to 600 °C and 3 %–30 % H_2O in H_2. It has to be mentioned that infiltration of nitrate solutions could lead to a change in the porosity of the electrode [116] followed by an increase of the gas diffusion resistance inside the electrode. Since the amount of infiltrated nickel in our electrodes is rather low, the change in the porosity and therefore the influence on the impedance is neglectable as shown in Fig. 4 where the lowest frequency peak of MC-B-46 and MC-B-23 is identical while the nickel amount is different (Table 1).

TABLE B.1
Microstructural parameters of GDC fuel electrode

Parameter	Symbol/unit	Value
Material fraction GDC	ε_{GDC}/-	0.75
Tortuosity of GDC	τ_{GDC}/-	1.31
Electrode thickness	L_{fe}/μm	5.3
Porosity	ε_{pore}/-	0.25
Tortuosity of pores	τ_{pore}/-	2.92
Pore diameter	d_{pore} (D50)/μm	0.08

Appendix C
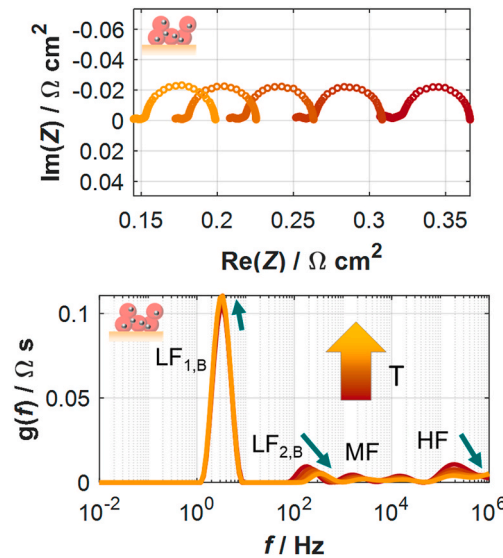
Fig. C.1. Temperature variation between 750 and 850 °C at 97 % / 3 % H_2/H_2O ($\Delta T = 25$ K) of MC-B-46 shows a slightly negative activation of the peak LF$_{1,B}$ which is typical for a gas diffusion process [50]. Compared to the temperature variation between 600 °C and 700 °C even the capacity of this process seems not to be activated by temperature. This could lead to the assumption that at lower operating temperatures peak LF$_{2,B}$ impacts the behavior of LF$_{1,B}$ due to a smaller difference in relaxation frequency. The presented measurements are not included in the characterization of the electrode since they are overlapped by minor ageing most probably due to high operating temperature.

Appendix D
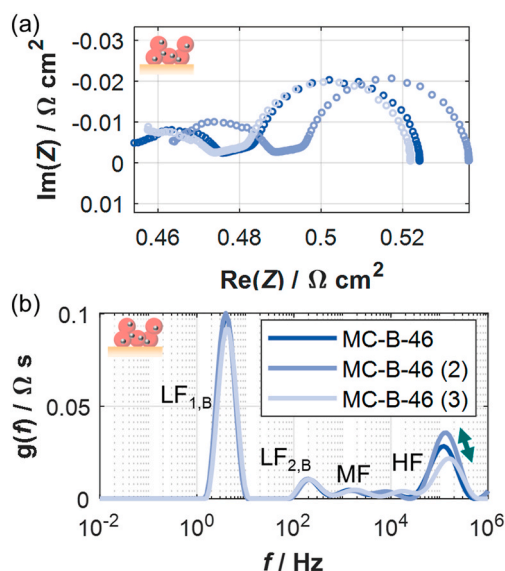
Fig. D.1. For reproducibility test of the electrodes, three cells with an MC-B-46 electrode are measured at 700 °C at 97 % / 3 % H_2/H_2O. High reproducibility is given at frequencies <10 kHz. Differences at frequencies >10 kHz are not explainable so far and are out of scope of this work. The peak $LF_{2,B}$ which is focus of this work shows high reproducibility. Differences in the ohmic resistance are explainable by the tolerance of the electrolyte thickness.

Data availability

Data can be found under the DOI: 10.35097/bf7zru2typhgnd7m.

References

[1] F. Han, M. Lang, P. Szabo, C. Geipel, C. Walter, R. Costa, Performance and degradation of electrolyte supported SOECs with advanced thin-flm gadolinium doped ceria barrier layers in long-term Stack test, J. Electrochem. Soc. 171 (2024) 054515, https://doi.org/10.1149/1945-7111/ad4781.

[2] Z. Wang, Y. Li, J.W. Schwank, Evaluation of Ni/SDC as anode material for dry CH4 fueled solid oxide fuel cells, J. Power Sources 248 (2014) 239–245, https://doi.org/10.1016/j.jpowsour.2013.09.043.

[3] M. Mogensen, T. Lindegaard, U.R. Hansen, G. Mogensen, Physical properties of mixed conductor solid oxide fuel cell anodes of doped CeO2, J. Electrochem. Soc. 141 (1994) 2122–2128, https://doi.org/10.1149/1.2055072.

[4] M. Mogensen, J.J. Bentzen, Oxidation of methane on oxide electrodes at 800–1000°C, Proc. - Electrochem. Soc. PV 1989–19 (1989) 99–110, https://doi.org/10.1149/198911.0099pv.

[5] S. Kavurucu Schubert, M. Kusnezoff, A. Michaelis, S.I. Bredikhin, Comparison of the performances of single cell solid oxide fuel cell stacks with Ni/8YSZ and Ni/10CGO anodes with H 2S containing fuel, J. Power Sources 217 (2012) 364–372, https://doi.org/10.1016/j.jpowsour.2012.06.020.

[6] C. Xu, P. Gansor, J.W. Zondlo, K. Sabolsky, E.M. Sabolsky, An H2S-tolerant Ni-GDC anode with a GDC barrier layer, J. Electrochem. Soc. 158 (2011) B1405–B1416, https://doi.org/10.1149/2.067111jes.

[7] B. Mirfakhraei, S. Paulson, V. Thangadurai, V. Birss, Enhanced hydrogen oxidation activity and H2S tolerance of Ni-infiltrated ceria solid oxide fuel cell anodes, J. Power Sources 243 (2013) 95–101, https://doi.org/10.1016/j.jpowsour.2013.05.150.

[8] T. Hays, A.M. Hussain, Y.L. Huang, D.W. McOwen, E.D. Wachsman, Improved sulfur tolerance of SOFCs through surface modification of anodes, ACS Appl. Energy Mater. 1 (2018) 1559–1566, https://doi.org/10.1021/acsaem.7b00354.

[9] S. Primdahl, Y.L. Liu, Ni catalyst for hydrogen conversion in gadolinia-doped ceria anodes for solid oxide fuel cells, J. Electrochem. Soc. 149 (2002) A1466–A1472, https://doi.org/10.1149/1.1514234.

[10] O.A. Marina, C. Bagger, S. Primdahl, M. Mogensen, A solid oxide fuel cell with a gadolinia-doped ceria anode: preparation and performance, Solid State Ionics 123 (1999) 199–208, https://doi.org/10.1016/S0167-2738(99)00111-3.

[11] J. Uecker, I.D. Unachukwu, V. Vibhu, I.C. Vinke, L.G.J. (Bert de Haart, R.-A. Eichel, Gadolinium doped ceria as nickel free fuel electrode in high temperature CO2-electrolysis, Chem. Electr.Chem. (2024) e202300617, https://doi.org/10.1002/celc.202300617.

[12] A. Shaur, M. Drazkowski, S. Zhu, B. Boukamp, H.J.M. Bouwmeester, A single-phase gadolinium-doped ceria cathode for highly efficient CO2 electrolysis, J. Mater. Chem. A 11 (2023) 25020–25030, https://doi.org/10.1039/d3ta03977c.

[13] A. Weber, T. Dickel, E. Ivers-Tiffée, Sulfur-tolerance of ceria-based anodes, 12th Eur. SOFC SOE Forum (2016) B0507.

[14] H. Uchida, N. Mochizuki, M. Watanabe, High-performance electrode for medium-temperature operating solid oxide fuel cells: polarization property of ceria-based anode with highly dispersed ruthenium catalysts in gas, J. Electrochem. Soc. 143 (1996) 1700–1704, https://doi.org/10.1149/1.1836703.

[15] M. Watanabe, H. Uchida, M. Shibata, N. Mochizuki, K. Amikura, High performance catalyzed-reaction layer for medium temperature operating solid oxide fuel cells, J. Electrochem. Soc. 141 (1994) 342–346, https://doi.org/10.1149/1.2054728.

[16] M.J. Saeki, H. Uchida, M. Watanabe, Noble metal catalysts highly-dispersed on Sm-doped ceria for the application to internal reforming solid oxide fuel cells operated at medium temperature, Catal. Lett. 26 (1994) 149–157, https://doi.org/10.1007/BF00824040.

[17] H. Uchida, S. Suzuki, M. Watanabe, High - performance electrode for medium - temperature solid oxide fuel cells : effects of composition and microstructures on performance of ceria - based anodes, J. Electrochem. Soc. 145 (1998) 615–620, https://doi.org/10.1149/1.1838312.

[18] F. Kullmann, A. Schwiers, M. Juckel, N.H. Menzler, A. Weber, Influence of microstructure on the sulfur tolerance of ceria-based anodes in low temperature SOFC, ECS Trans. 111 (2023) 1013–1023, https://doi.org/10.1149/11106.1013ecst.

[19] F. Kullmann, A. Schwiers, M. Juckel, N.H. Menzler, A. Weber, Enhancement of performance and sulfur tolerance of ceria-based fuel electrodes in low temperature SOFC, J. Electrochem. Soc. 171 (2024) 044511, https://doi.org/10.1149/1945-7111/ad3ebd.

[20] R. Leah, A. Bone, M. Lankin, A. Selcuk, R. Pierce, L. Rees, D. Corcoran, P. Muhl, Z. Dehaney-Steven, C. Brackenbury, M. Selby, S. Mukerjee, Low-cost, REDOX-stable, low-temperature SOFC developed by ceres power for multiple applications: latest development update, ECS Trans. 57 (2013) 461–470, https://doi.org/10.1149/05701.0461ecst.

[21] R. Leah, A. Bone, P. Hjalmarsson, A. Selcuk, M. Lankin, M. Rahman, A. Clare, G. Reade, F. Felix, J. De Vero, Xi Wang, S. Mukerjee, M. Selby, Commercialization of the ceres power SteelCell ® technology: latest update, ECS Trans. 103 (2021) 679–684, https://doi.org/10.1149/10301.0679ecst.

[22] K.T. Lee, E.D. Wachsman, Role of nanostructures on SOFC performance at reduced temperatures, MRS Bull. 39 (2014) 783–791, https://doi.org/10.1557/mrs.2014.193.

[23] I. Robinson, Y. Huang, S.A. Horlick, A.M. Hussain, A. Pesaran, E.D. Wachsman, Enhancing low-temperature SOFC performance and durability via surface modification, ECS Trans. 111 (2023) 47–50, https://doi.org/10.1149/11106.0047ecst.

[24] A.M. Abdalla, S. Hossain, A.T. Azad, P.M.I. Petra, F. Begum, S.G. Eriksson, A. K. Azad, Nanomaterials for solid oxide fuel cells: a review, Renew. Sustain. Energy Rev. 82 (2018) 353–368, https://doi.org/10.1016/j.rser.2017.09.046.

[25] A. Weber, S. Dierickx, N. Russner, E. Ivers-Tiffée, Sulfur poisoning of Ni-based SOFC-anodes – short and long term behavior, ECS Trans. 77 (2017) 141–147, https://doi.org/10.1149/07710.0141ecst.

[26] S. Primdahl, M.B. Mogensen, Mixed conductor anodes: Ni as electrocatalyst for hydrogen conversion, Solid State Ionics 152–153 (2002) 597–608, https://doi.org/10.1016/S0167-2738(02)00393-4.

[27] J.W. Yun, S.P. Yoon, J. Han, S. Park, H.S. Kim, S.W. Nam, Ceria coatings effect on H[sub 2]S poisoning of Ni/YSZ anodes for solid oxide fuel cells, J. Electrochem. Soc. 157 (2010) B1825–B1830, https://doi.org/10.1149/1.3499215.

[28] S.P. Jiang, Nanoscale and nano-structured electrodes of solid oxide fuel cells by infiltration: advances and challenges, Int. J. Hydrogen Energy 37 (2012) 449–470, https://doi.org/10.1016/j.ijhydene.2011.09.067.

[29] A. Babaei, S.P. Jiang, J. Li, Electrocatalytic promotion of palladium nanoparticles on hydrogen oxidation on Ni/GDC anodes of SOFCs via spillover, J. Electrochem. Soc. 156 (2009) B1022–B1029, https://doi.org/10.1149/1.3156637.

[30] J. Nielsen, B.R. Sudireddy, A. Hagen, Å.H. Persson, Performance factors and sulfur tolerance of metal supported solid oxide fuel cells with nanostructured Ni: GDC infiltrated anodes, J. Electrochem. Soc. 163 (2016) F574–F580, https://doi.org/10.1149/2.1081606jes.

[31] X. Ding, W. Zhu, G. Hua, J. Li, Z. Wu, Enhanced oxygen reduction activity on surface-decorated perovskite La0.6Ni0.4FeO3 cathode for solid oxide fuel cells, Electrochim. Acta 163 (2015) 204–212, https://doi.org/10.1016/j.electacta.2015.02.084.

[32] D. Ding, X. Li, S.Y. Lai, K. Gerdes, M. Liu, Enhancing SOFC cathode performance by surface modification through infiltration, Energy Environ. Sci. 7 (2014) 552–575, https://doi.org/10.1039/c3ee42926a.

[33] D. Ding, M. Liu, Z. Liu, X. Li, K. Blinn, X. Zhu, M. Liu, Efficient electro-catalysts for enhancing surface activity and stability of SOFC cathodes, Adv. Energy Mater. 3 (2013) 1149–1154, https://doi.org/10.1002/aenm.201200984.

[34] R. Kiebach, C. Knöfel, F. Bozza, T. Klemensø, C. Chatzichristodoulou, Infiltration of ionic-, electronic- and mixed-conducting nano particles into La0.75Sr0.25MnO3-Y0.16Zr 0.84O2 cathodes-A comparative study of performance enhancement and stability at different temperatures, J. Power Sources 228 (2013) 170–177, https://doi.org/10.1016/j.jpowsour.2012.11.070.

[35] T. Klemensø, C. Chatzichristodoulou, J. Nielsen, F. Bozza, K. Thydén, R. Kiebach, S. Ramousse, Characterization of impregnated GDC nano structures and their functionality in LSM based cathodes, Solid State Ionics 224 (2012) 21–31, https://doi.org/10.1016/j.ssi.2012.07.011.

[36] D.A. Osinkin, Hydrogen oxidation kinetics on a redox stable electrode for reversible solid-state electrochemical devices: the critical influence of hydrogen dissociation on the electrode surface, Electrochim. Acta 389 (2021) 138792, https://doi.org/10.1016/j.electacta.2021.138792.

[37] D.A. Osinkin, Complementary effect of ceria on the hydrogen oxidation kinetics on Ni - Ce0.8Sm0.2O2-δ anode, Electrochim. Acta 330 (2020) 135257, https://doi.org/10.1016/j.electacta.2019.135257.

[38] D.A. Osinkin, Boosting electrochemical performance of Ni/YSZ electrode through simultaneous injection of nickel and ceria, Int. J. Hydrogen Energy 82 (2024) 1222–1229, https://doi.org/10.1016/j.ijhydene.2024.08.083.

[39] D.A. Osinkin, The parallel pathways of hydrogen oxidation reaction on high active decorated Ni–YSZ electrode in electrochemical cell with GDC protective layer, J. Electroanal. Chem. 927 (2022) 116999, https://doi.org/10.1016/j.jelechem.2022.116999.

[40] D.A. Osinkin, Detailed analysis of electrochemical behavior of high–performance solid oxide fuel cell using DRT technique, J. Power Sources 527 (2022) 231120, https://doi.org/10.1016/j.jpowsour.2022.231120.

[41] F. Kullmann, M. Mueller, A. Lindner, S. Dierickx, E. Mueller, A. Weber, DRT analysis and transmission line modeling of ceria based electrodes for solid oxide cells, J. Power Sources 587 (2023) 233706, https://doi.org/10.1016/j.jpowsour.2023.233706.

[42] J. Nielsen, J. Hjelm, Impedance of SOFC electrodes: a review and a comprehensive case study on the impedance of LSM:YSZ cathodes, Electrochim. Acta 115 (2014) 31–45, https://doi.org/10.1016/j.electacta.2013.10.053.

[43] J. Nielsen, T. Klemenso, P. Blennow, Detailed impedance characterization of a well performing and durable Ni:CGO infiltrated cermet anode for metal-supported solid oxide fuel cells, J. Power Sources 219 (2012) 305–316, https://doi.org/10.1016/j.jpowsour.2012.07.031.

[44] S. Dierickx, T. Mundloch, A. Weber, E. Ivers-Tiffée, Advanced impedance model for double-layered solid oxide fuel cell cermet anodes, J. Power Sources 415 (2019) 69–82, https://doi.org/10.1016/j.jpowsour.2019.01.043.

[45] A. Nenning, C. Bischof, J. Fleig, M. Bram, A.K. Opitz, The relation of microstructure, materials properties and impedance of SOFC electrodes: a case study of Ni/GDC anodes, Energies 13 (2020) 987, https://doi.org/10.3390/en13040987.

[46] S. Dierickx, J. Joos, A. Weber, E. Ivers-Tiffée, Advanced impedance modelling of Ni/8YSZ cermet anodes, Electrochim. Acta 265 (2018) 736–750, https://doi.org/10.1016/j.electacta.2017.12.029.

[47] E.C. Shin, J. Ma, P.A. Ahn, H.H. Seo, D.T. Nguyen, J.S. Lee, Deconvolution of four transmission-line-model impedances in Ni-YSZ/YSZ/LSM solid oxide cells and mechanistic insights, Electrochim. Acta 188 (2016) 240–253, https://doi.org/10.1016/j.electacta.2015.11.118.

[48] D. Udomsilp, J. Rechberger, R. Neubauer, C. Bischof, F. Thaler, W. Schafbauer, N. H. Menzler, L.G.J. de Haart, A. Nenning, A.K. Opitz, O. Guillon, M. Bram, Metal-supported solid oxide fuel cells with exceptionally high power density for range extender systems, Cell Rep. Phys. Sci. 1 (2020) 1–17, https://doi.org/10.1016/j.xcrp.2020.100072.

[49] J. Nielsen, P. Hjalmarsson, M.H. Hansen, P. Blennow, Effect of low temperature in-situ sintering on the impedance and the performance of intermediate temperature solid oxide fuel cell cathodes, J. Power Sources 245 (2014) 418–428, https://doi.org/10.1016/j.jpowsour.2013.06.067.

[50] V. Sonn, A. Leonide, E. Ivers-Tiffée, Combined deconvolution and CNLS fitting approach applied on the impedance response of technical Ni/8YSZ cermet electrodes, J. Electrochem. Soc. 155 (2008) B675–B679, https://doi.org/10.1149/1.2908860.

[51] R. Mohammadi, M. Søgaard, T. Ramos, M. Ghassemi, M.B. Mogensen, Electrochemical impedance modeling of a solid oxide fuel cell anode, Fuel Cell. 14 (2014) 645–659, https://doi.org/10.1002/fuce.201300292.

[52] E.C. Shin, P.A. Ahn, H.H. Seo, D.T. Nguyen, S.D. Kim, S.K. Woo, J.H. Yu, J.S. Lee, Pinning-down polarization losses and electrode kinetics in cermet-supported LSM solid oxide cells in reversible operation, Solid State Ionics 277 (2015) 1–10, https://doi.org/10.1016/j.ssi.2015.04.009.

[53] T. Kawada, N. Sakai, H. Yokokawa, M. Dokiya, M. Mori, T. Iwata, Structure and polarization characteristics of solid oxide fuel cell anodes, Solid State Ionics 40–41 (1990) 402–406, https://doi.org/10.1016/0167-2738(90)90367-Z.

[54] D. Esau, C. Grosselindemann, S.P. Sckuhr, F. Kullmann, A. Lindner, Z. Liang, F. M. Fuchs, A. Weber, Electrochemical characterization of nickel/gadolinia doped ceria fuel electrodes under H2/H2O/CO/CO2-atmospheres, J. Electrochem. Soc. 171 (2024) 054522, https://doi.org/10.1149/1945-7111/ad4c10.

[55] A. Sciazko, Y. Komatsu, T. Shimura, Y. Sunada, N. Shikazono, Correlation between microstructure and performance of GDC-based electrodes, ECS Trans. 111 (2023) 349–356, https://doi.org/10.1149/11106.0349ecst.

[56] D. Klotz, A. Weber, E. Ivers-Tiffée, Practical guidelines for reliable electrochemical characterization of solid oxide fuel cells, Electrochim. Acta 227 (2017) 110–126, https://doi.org/10.1016/j.electacta.2016.12.148.

[57] L. Holzer, B. Iwanschitz, T. Hocker, B. Münch, M. Prestat, D. Wiedenmann, U. Vogt, P. Holtappels, J. Sfeir, A. Mai, T. Graule, Microstructure degradation of cermet anodes for solid oxide fuel cells: quantification of nickel grain growth in dry and in humid atmospheres, J. Power Sources 196 (2011) 1279–1294, https://doi.org/10.1016/j.jpowsour.2010.08.017.

[58] M. Schönleber, D. Klotz, E. Ivers-Tiffée, A method for improving the robustness of linear kramers-kronig validity tests, Electrochim. Acta 131 (2014) 20–27, https://doi.org/10.1016/j.electacta.2014.01.034.

[59] B.A. Boukamp, A linear kronig-kramers transform test for immittance data validation, J. Electrochem. Soc. 142 (1995) 1885–1894, https://doi.org/10.1149/1.2044210.

[60] H. Schichlein, A.C. Müller, M. Voigts, A. Krügel, E. Ivers-Tiffée, Deconvolution of electrochemical impedance spectra for the identification of electrode reaction mechanisms in solid oxide fuel cells, J. Appl. Electrochem. 32 (2002) 875, https://doi.org/10.1023/A:1020599525160.

[61] B.A. Boukamp, A nonlinear least square fit procedure for analysis of immittance data of electrochemical systems, Solid State Ionics 20 (1986) 31–44, https://doi.org/10.1016/0167-2738(86)90031-7.

[62] J. Weese, A reliable and fast method for the solution of Fredholm integral equations of the first kind based on Tikhonov regularization, Comput. Phys. Commun. 69 (1992) 99–111, https://doi.org/10.1016/0010-4655(92)90132-I.

[63] S. Dierickx, A. Weber, E. Ivers-Tiffée, How the distribution of relaxation times enhances complex equivalent circuit models for fuel cells, Electrochim. Acta 355 (2020) 136764, https://doi.org/10.1016/j.electacta.2020.136764.

[64] J. Euler, W. Nonnenmacher, Stromverteilung in porösen elektroden, Electrochim. Acta 2 (1960) 268–286, https://doi.org/10.1016/0013-4686(60)80025-4.

[65] R.D. Levie, On porous electrodes in electrolyte solutions-IV, Electrochim. Acta 9 (1964) 1231–1245, https://doi.org/10.1016/0013-4686(64)85015-5.

[66] J. Bisquert, G. Garcia-Belmonte, F. Fabregat-Santiago, A. Compte, Anomalous transport effects in the impedance of porous film electrodes, Electrochem. Commun. 1 (1999) 429–435, https://doi.org/10.1016/S1388-2481(99)00084-3.

[67] M.E. Orazem, B. Tribollet, Electrochemical Impedance Spectroscopy, John Wiley and Sons Inc, 2017.

[68] S.R. Bishop, K.L. Duncan, E.D. Wachsman, Surface and bulk oxygen non-stoichiometry and bulk chemical expansion in gadolinium-doped cerium oxide, Acta Mater. 57 (2009) 3596–3605, https://doi.org/10.1016/j.actamat.2009.04.017.

[69] W.G. Bessler, S. Gewies, Gas concentration impedance of solid oxide fuel cell anodes, J. Electrochem. Soc. 154 (2007) B548, https://doi.org/10.1149/1.2720639.

[70] W.G. Bessler, Gas concentration impedance of solid oxide fuel cell anodes, J. Electrochem. Soc. 153 (2006) A1492, https://doi.org/10.1149/1.2205150.

[71] W.G. Bessler, Gas concentration impedance of SOFC anodes. Proc. 7th Eur. Solid Oxide Fuel Cell Forum, 2006. P0707.

[72] S. Primdahl, M. Mogensen, Gas diffusion impedance in characterization of solid oxide fuel cell anodes, J. Electrochem. Soc. 146 (1999) 2827–2833, https://doi.org/10.1149/1.1392015.

[73] S. Primdahl, M. Mogensen, Gas conversion impedance: a test geometry effect in characterization of solid oxide fuel cell anodes, J. Electrochem. Soc. 145 (1998) 2431–2438, https://doi.org/10.1149/1.1838654.

[74] A. Leonide, V. Sonn, A. Weber, E. Ivers-Tiffée, Evaluation and modeling of the cell resistance in anode-supported solid oxide fuel cells, J. Electrochem. Soc. 155 (2008) B36–B41, https://doi.org/10.1149/1.2801372.

[75] T. Ramos, M. Søgaard, M.B. Mogensen, Electrochemical characterization of Ni/ScYSZ electrodes as SOFC anodes, J. Electrochem. Soc. 161 (2014) F434–F444, https://doi.org/10.1149/2.045404jes.

[76] C. Grosselindemann, N. Russner, S. Dierickx, F. Wankmüller, A. Weber, Deconvolution of gas diffusion polarization in Ni/Gadolinium-Doped ceria fuel electrodes, J. Electrochem. Soc. 168 (2021) 124506, https://doi.org/10.1149/1945-7111/ac3d02.

[77] M. Riegraf, R. Costa, G. Schiller, K.A. Friedrich, S. Dierickx, A. Weber, Electrochemical impedance analysis of symmetrical Ni/Gadolinium-Doped ceria (CGO10) electrodes in electrolyte-supported solid oxide cells, J. Electrochem. Soc. 166 (2019) F865–F872, https://doi.org/10.1149/2.0051913jes.

[78] T. Ramosa, K. Thydéna, M. Mogensen, Electrochemical characterization of Ni/(Sc) YSZ electrodes, ECS Trans. 28 (2010) 123–139, https://doi.org/10.1149/1.3495837.

[79] F. Kullmann, C. Grosselindemann, L. Salamon, F.-M. Fuchs, A. Weber, Impedance analysis of electrolyte processes in a solid oxide cell, Fuel Cell. 1 (2023) 1–9, https://doi.org/10.1002/fuce.202300035.

[80] M. Li, W. Yin, J. Pan, Y. Zhu, N. Sun, X. Zhang, Y. Wan, Z. Luo, L. Yi, L. Wang, Hydrogen spillover as a promising strategy for boosting heterogeneous catalysis and hydrogen storage, Chem. Eng. J. 471 (2023) 144691, https://doi.org/10.1016/j.cej.2023.144691.

[81] Y. Liu, M. Juckel, N.H. Menzler, A. Weber, Ni/GDC fuel electrode for low temperature SOFC and its aging behavior under accelerated stress, ECS Trans. 111 (2023) 1855, https://doi.org/10.1149/11106.1855ecst.

[82] M. Riegraf, V. Yurkiv, R. Costa, G. Schiller, K.A. Friedrich, Evaluation of the effect of sulfur on the performance of nickel/gadolinium-doped ceria based solid oxide fuel cell anodes, ChemSusChem 10 (2017) 587–599, https://doi.org/10.1002/cssc.201601320.

[83] N. Mazzanti, Ceria-based thin film electrodes for sustainable hydrogen production, DTU Energy (2021).

[84] W.C. Chueh, Y. Hao, W. Jung, S.M. Haile, High electrochemical activity of the oxide phase in model ceria-Pt and ceria-Ni composite anodes, Nat. Mater. 11 (2012) 155–161, https://doi.org/10.1038/nmat3184.

[85] W. Jung, K.L. Gu, Y. Choi, S.M. Haile, Robust nanostructures with exceptionally high electrochemical reaction activity for high temperature fuel cell electrodes, Energy Environ. Sci. 7 (2014) 1685–1692, https://doi.org/10.1039/c3ee43546f.

[86] J. Uecker, I.D. Unachukwu, V. Vibhu, I.C. Vinke, R.A. Eichel, L.G.J. (Bert, de Haart, Performance, electrochemical process analysis and degradation of gadolinium doped ceria as fuel electrode material for solid oxide electrolysis cells, Electrochim. Acta 452 (2023) 142320, https://doi.org/10.1016/j.electacta.2023.142320.

[87] S.P.S. Badwal, Effect of dopant concentration on the grain boundary and volume resistivity of yttria-zirconia, J. Mater. Sci. Lett. 6 (1987) 1419–1421, https://doi.org/10.1007/BF01689307.

[88] J.E. Bauerle, Study of solid electrolyte polarization by a complex admittance method, J. Phys. Chem. Solid. 30 (1969) 2657, https://doi.org/10.1016/0022-3697(69)90039-0.

[89] S. Golani, F. Wankmüller, W. Herzhof, C. Dellen, N.H. Menzler, A. Weber, Impact of GDC interlayer microstructure on strontium zirconate interphase formation and cell performance, 15th Eur. SOFC SOE Forum (2022) A0901.

[90] A. Tsoga, A. Naoumidis, D. Stöver, Total electrical conductivity and defect structure of ZrO2-CeO2-Y2O3-Gd2O3 solid solutions, Solid State Ionics 135 (2000) 403–409, https://doi.org/10.1016/S0167-2738(00)00477-X.

[91] A. Tsoga, A. Naoumidis, A. Gupta, D. Stöver, Microstructure and interdiffusion phenomena in YSZ-CGO composite electrolyte, Mater. Sci. Forum (1999) 308–311. https://doi.org/10.4028/www.scientific.net/msf.308-311.794, 794–799.

[92] J. Szász, F. Wankmüller, V. Wilde, H. Störmer, D. Gerthsen, N.H. Menzler, E. Ivers-Tiffée, Nature and functionality of La 0.58 Sr 0.4 Co 0.2 Fe 0.8 O 3-δ/Gd 0.2 Ce 0.8 O 2-δ/Y 0.16 Zr 0.84 O 2-δ interfaces in SOFCs, J. Electrochem. Soc. 165 (2018) F898–F906, https://doi.org/10.1149/2.0031811jes.

[93] A. Hagen, A.K. Padinjarethil, J. Heijne, Experimental deconvolution of resistance contributions in commercial solid oxide cells with Ni-CGO electrode, Electrochim. Acta 461 (2023) 142672, https://doi.org/10.1016/j.electacta.2023.142672.

[94] V.A. Rojek-Wöckner, A.K. Opitz, M. Brandner, J. Mathé, M. Bram, A novel Ni/ceria-based anode for metal-supported solid oxide fuel cells, J. Power Sources 328 (2016) 65–74, https://doi.org/10.1016/j.jpowsour.2016.07.075.

[95] E. Brightman, D.G. Ivey, D.J.L. Brett, N.P. Brandon, The effect of current density on H2S-poisoning of nickel-based solid oxide fuel cell anodes, J. Power Sources 196 (2011) 7182–7187, https://doi.org/10.1016/j.jpowsour.2010.09.089.

[96] A. Kromp, S. Dierickx, A. Leonide, A. Weber, E. Ivers-Tiffée, Electrochemical analysis of sulfur-poisoning in anode supported SOFCs fuelled with a model reformate, J. Electrochem. Soc. 159 (2012) B597–B601, https://doi.org/10.1149/2.015206jes.

[97] J.B. Hansen, Correlating sulfur poisoning of SOFC nickel anodes by a temkin isotherm, Electrochem, Solid-State Lett. 11 (2008) B178, https://doi.org/10.1149/1.2960521.

[98] D.R. Huntley, The decomposition of H2S on Ni(110), Surf. Sci. 240 (1990) 13–23, https://doi.org/10.1016/0039-6028(90)90726-O.

[99] C.H. Bartholomew, Mechanisms of catalyst deactivation, Appl. Catal. Gen. 212 (2001) 17–60, https://doi.org/10.1016/S0926-860X(00)00843-7.

[100] J.F.B. Rasmussen, A. Hagen, The effect of H2S on the performance of Ni-YSZ anodes in solid oxide fuel cells, J. Power Sources 191 (2009) 534–541, https://doi.org/10.1016/j.jpowsour.2009.02.001.

[101] A. Hauch, A. Hagen, J. Hjelm, T. Ramos, Sulfur poisoning of SOFC anodes: effect of overpotential on long-term degradation, J. Electrochem. Soc. 161 (2014) F734–F743, https://doi.org/10.1149/2.080406jes.

[102] L. Zhang, S.P. Jiang, H.Q. He, X. Chen, J. Ma, X.C. Song, A comparative study of H2S poisoning on electrode behavior of Ni/YSZ and Ni/GDC anodes of solid oxide fuel cells, Int. J. Hydrogen Energy 35 (2010) 12359–12368, https://doi.org/10.1016/j.ijhydene.2010.08.067.

[103] P. Lohsoontorn, D.J.L. Brett, N.P. Brandon, The effect of fuel composition and temperature on the interaction of H2S with nickel-ceria anodes for Solid Oxide Fuel Cells, J. Power Sources 183 (2008) 232–239, https://doi.org/10.1016/j.jpowsour.2008.04.021.

[104] M. Riegraf, R. Costa, G. Schiller, K.A. Friedrich, Sulfur poisoning of Ni/CGO anodes: a long-term degradation study, ECS Trans. 78 (2017) 1285–1291, https://doi.org/10.1149/07801.1285ecst.

[105] M. Riegraf, M.P. Hoerlein, R. Costa, G. Schiller, K.A. Friedrich, Sulfur poisoning of electrochemical reformate conversion on nickel/gadolinium-doped ceria electrodes, ACS Catal. 7 (2017) 7760–7771, https://doi.org/10.1021/acscatal.7b02177.

[106] S.B. Adler, Mechanism and kinetics of oxygen reduction on porous La1-xSrxCoO3-δ electrodes, Solid State Ionics 111 (1998) 125–134, https://doi.org/10.1016/s0167-2738(98)00179-9.

[107] J. Nielsen, T. Jacobsen, M. Wandel, Impedance of porous IT-SOFC LSCF:CGO composite cathodes, Electrochim. Acta 56 (2011) 7963–7974, https://doi.org/10.1016/j.electacta.2011.05.042.

[108] W.C. Chueh, S.M. Haile, Electrochemical studies of capacitance in cerium oxide thin films and its relationship to anionic and electronic defect densities, Phys. Chem. Chem. Phys. 11 (2009) 8144–8148, https://doi.org/10.1039/b910903j.

[109] E.M. Sala, N. Mazzanti, F.M. Chiabrera, S. Sanna, M.B. Mogensen, P. V. Hendriksen, Z. Ma, S.B. Simonsen, C. Chatzichristodoulou, Unravelling the role of dopants in the electrocatalytic activity of ceria towards CO2 reduction in solid oxide electrolysis cells, Phys. Chem. Chem. Phys. 25 (2023) 3457–3471, https://doi.org/10.1039/d2cp05157e.

[110] D. Chen, S.R. Bishop, H.L. Tuller, Nonstoichiometry in oxide thin films operating under anodic conditions: a chemical capacitance study of the praseodymium-cerium oxide system, Chem. Mater. 26 (2014) 6622–6627, https://doi.org/10.1021/cm503440v.

[111] Z.A. Feng, F. El Gabaly, X. Ye, Z.X. Shen, W.C. Chueh, Fast vacancy-mediated oxygen ion incorporation across the ceria-gas electrochemical interface, Nat. Commun. 5 (2014) 4374, https://doi.org/10.1038/ncomms5374.

[112] N.J. Williams, I.D. Seymour, R.T. Leah, A. Banerjee, S. Mukerjee, S.J. Skinner, Non-equilibrium thermodynamics of mixed ionic-electronic conductive electrodes and their interfaces: a Ni/CGO study, J. Mater. Chem. A 10 (2022) 11121–11130, https://doi.org/10.1039/d1ta07351f.

[113] A. Leonide, Y. Apel, E. Ivers-Tiffee, SOFC modeling and parameter identification by means of impedance spectroscopy, ECS Trans. 19 (2009) 81–109, https://doi.org/10.1149/1.3247567.

[114] GeoDict software, Release 2023 from Math2Market GmbH, Ger. (n.d.). https://www.geodict.com. .

[115] N. Epstein, On tortuosity and the tortuosity factor in flow and diffusion through porous media, Chem. Eng. Sci. 44 (1989) 777–779, https://doi.org/10.1016/0009-2509(89)85053-5.

[116] D.A. Osinkin, Identification of gas diffusion phenomena on highly active Ni–ceramic anodes using the DRT technique, J. Power Sources 571 (2023) 233085, https://doi.org/10.1016/j.jpowsour.2023.233085.